Experimental and numerical study of sooting tendency of IBE in a laminar diffusion flame

by

Abhee Singh

A thesis submitted to the Graduate Faculty of
Auburn University
in partial fulfillment of the
requirements for the Degree of
Master of Science in Mechanical Engineering

Auburn, Alabama
August 06, 2022

Keywords: Isopropanol-butanol-ethanol, laminar diffusion flame, soot, YSI, color ratio pyrometry

Approved by

Nicholas Tsolas, Chair, Assistant Professor, Mechanical Engineering
Sushil Adhikari, Professor, Biosystems Engineering
Mark Hoffman, Assistant Professor, Mechanical Engineering

Abstract

Recent advancements in metabolic engineering have demonstrated that through cost-effective batch fermentation processes, isopropanol-butanol-ethanol (IBE) can be produced at sufficient quantities from switchgrass biomass. As such, IBE is seen as a promising third-generation biofuel candidate that can potentially address the inadequacies of its predecessor, acetone-butanol-ethanol (ABE), which was known to corrode engine parts. Previous studies have shown that when IBE is blended with diesel at proportions as high as 40% by volume, it can retain favorable spray and combustion characteristics while exhibiting lower sooting tendencies. However, there is not only a lack of experimental data demonstrating reduced sooting of IBE with diesel blends, but also a lack of understanding of how IBE kinetically contributes to lowering soot formation. In this study, the soot reduction potential of IBE when mixed with surrogate diesel (a binary mixture of 70% vol. of n-decane and 30% vol. 1-methylnaphthalene) is examined in an atmospheric co-flow diffusion flame burner. Furthermore, the individual effect of carbon and oxygen loading of IBE on its sooting tendency is studied by modifying its component ratio. Finally, the oxidizer stream of the burner is diluted with CO_2, thus replicating exhaust gas recirculation (EGR) system in a compression ignition (CI) engine and enabling to study its effect on total soot yield in the flame. Experimental measurements of soot volume fractions are obtained by a soot emission-based color-ratio pyrometry technique and the sooting tendency of different IBE-surrogate diesel blends is reported in terms of Yield Sooting Index (YSI). To gain further insight into the reaction chemistry affecting soot formation, experimental results are corroborated with numerical modelling results. Simulations are performed with a CFD laminar co-flow flame modelling solver, laminarSMOKE++ and a C1-C16 high

temperature kinetic mechanism including polycyclic aromatic hydrocarbons (PAH) and soot sub-modules. Through rate of production (ROP) analysis, dominant reaction pathways to soot formation are identified for different IBE-surrogate diesel blends at several CO_2 concentrations in the oxidizer stream as well as for various IBE component ratios. The major objectives of this research work were to benchmark an existent kinetic mechanism for its reliability to perform soot studies of IBE and study the chemical effect of IBE and CO_2 on traditional soot precursor formation pathways typically seen in diesel fuels.

Acknowledgments

I would initially like to extend sincere gratitude to my advisor, Dr. Nicholas Tsolas for providing an opportunity to work in his laboratory and initiate this research project. His continuous guidance and support was not only invaluable for the completion of this thesis but also helped me to navigate the process of undertaking quality research work. Special thanks to my committee members, Dr. Sushil Adhikari and Dr. Mark Hoffman for their insightful comments during my thesis defense which enlightened me on certain topics in this thesis.

I would like to express deep appreciation towards my laboratory colleagues, Karan Bopaiah, Jackson Jaworski, and Zane Oligee for their assistance during my research endeavours. It has truly been an amazing experience to work with you.

Finally, I would like to thank my family members for their love and support throughout this journey.

Table of Contents

List of Tables

List of Figures

List of Abbreviations

PM	Particulate Matter
ABE	Acetone-Butanol-Ethanol
IBE	Isopropanol-Butanol-Ethanol
EGR	Exhaust Gas Recirculation
CI	Compression Ignition
YSI	Yield Sooting Index
GHG	Greenhouse gas
LII	Laser Induced Incandescence
LIF	Laser Induced Flouroscence
TSI	Threshold Sooting Index
OESI	Oxygen Extended Sooting Index
PAH	Polycyclic aromatic hydrocarbon
HACA	Hydrogen abstraction carbon addition
MIT	Main injection timing
PIT	Pilot injection timing
FESI	Fuel Equivalent Sooting Index
MPI	Micropyrolysis Index
CRP	Color ratio pyrometry

CHAPTER 1: INTRODUCTION

1.1. Background and Motivation

Soot emissions majorly contribute to the particulate matter (PM) presence in the atmosphere and are mainly caused due to burning of hydrocarbon fuels. A report submitted by the Environmental Protection Agency (EPA) states that transportation is the most dominant contributor to total soot emissions in the US [1]. Several studies have found that long-term exposure to soot can lead to serious health effects. When microscopic particles like soot penetrate the lungs, they not only cause respiratory diseases such as asthma and bronchitis, but can contribute to increasing the risk of heart attacks and strokes [2]. A draft assessing the policy of air quality standards with respect to particulate matter, reports that close to 45,000 annual deaths in the US are linked to soot exposure [3]. More recently, it was also discovered that a strong correlation exists between soot exposure (particles less than 2.5 μm – see ***Figure 1***) and higher mortality rates associated with COVID-19 (see ***Figure 2***) [4].

Apart from health concerns, the severe impact of soot emissions on the environment are also well documented. A study conducted in 2013 found that soot is the second largest contributor to global warming after carbon dioxide [5]. When soot is present in the atmosphere or deposits on snow and ice surfaces, it can absorb solar irradiation more effectively and raise the environmental temperature of the surroundings. Atmospheric soot particles can also have an indirect effect on cloud formation behavior. Karcher et al. [6] found that when soot combines with sulfuric acid it can lead to the formation of ice crystals, thus making the clouds optically thicker. Such clouds are less permeable to radiation emitted by the Earth and can lead to higher atmospheric temperatures.

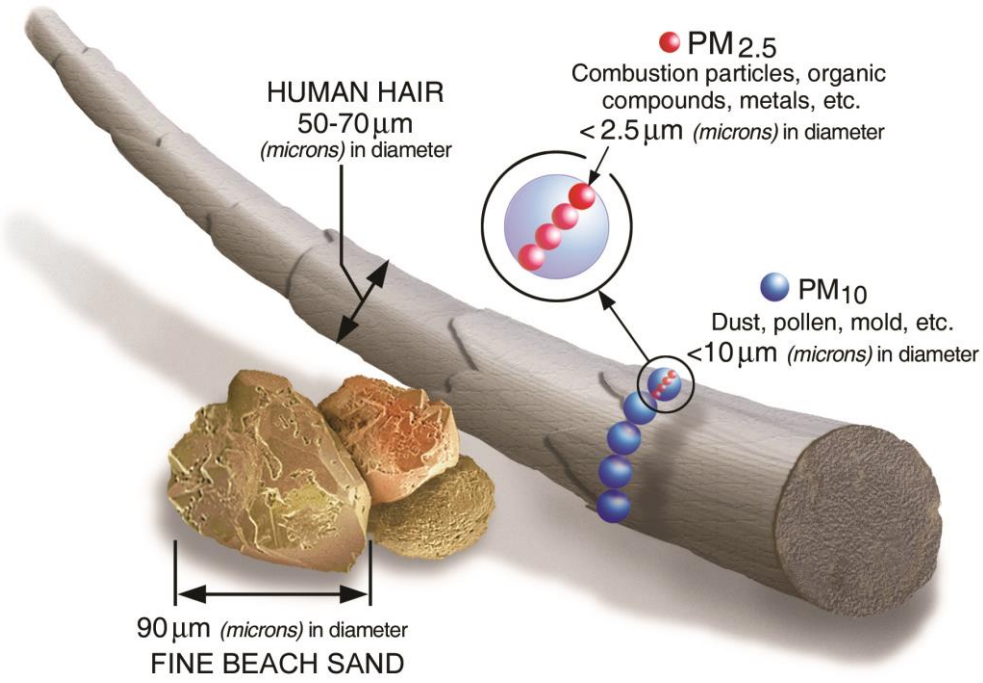

Figure 1: Illustration of soot particle size. (Adapted from: https://www.epa.gov/pm-pollution/particulate-matter-pm-basics)

In addition to climate change, soot emissions affect the environment by causing acidification of lakes and rivers. The mixture of soot and sulfur dioxide with atmospheric moisture can result in acid rain. Acid rain when carried by the wind can lower pH levels of lakes and rivers, which can lead to a deterioration of aquatic ecosystems and nutrient levels in the soil. This loss in soil nutrients can eventually damage trees by making them vulnerable to colder temperatures due to their inability to absorb sunlight.

Recognizing the severe health and environmental effects that soot can implicate, tremendous efforts have been made to limit its emission. For instance, the United States Department of Energy (DOE) introduced Co-Optimization of Fuels and Engines (Co-Optima) initiative to simultaneously investigate new fuels and engine technologies that are not only more energy efficient, but also produce less emissions, inclusing soot [7]. As part of this initiative, researchers have identified butanol as a promising biofuel candidate that can be blended with diesel with less environmental

[8]. Several other studies have supported the commercialization potential of bio-butanol due to its favorable fuel properties.

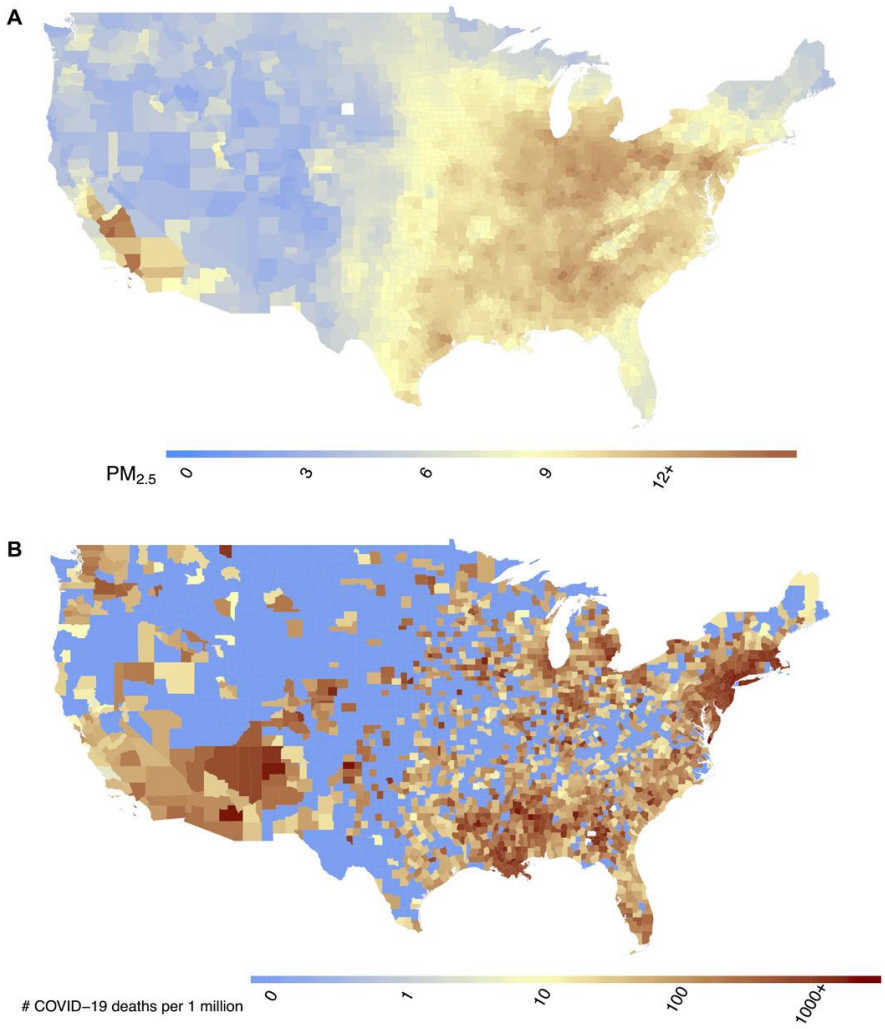

Figure 2: (A) PM2.5 concentrations in United States counties in µg/m^3 and (B) number of COVID-19 deaths per 1 million population. Adapted from [4]

Unlike its short-chain alcohol predecessors, methanol and ethanol, butanol has a longer hydrocarbon chain that enables it to have a higher cetane number and energy density, while exhibiting favorable combustion characteristics in terms of lower auto-ignition temperature and evaporation pressure. Combined with its higher miscibility with diesel, and lower hydroscopic and

corrosive tendencies, butanol is seen as a prime candidate to be used as a blending agent or direct fuel replacement in existing diesel engine architectures and infrastructures. However, the greatest drawback facing butanol implementation is the viability of current production methods. Generally, pure bio-butanol is extracted and purified through an intermediate, namely acetone-butanol-ethanol (ABE), during an anaerobic process of lignocellulosic feedstocks (e.g., wheat straw, bagasse, switch grass, corn straw and barley straw, etc.) using fermentation microorganisms [9]. The recovery techniques, however, which often involve a distillation process, are both energy intensive and costly, and often yield low production efficiency; makes butanol usage unfortunately less attractive in comparison to exiting petroleum-based fuels. To alleviate this burden and increase the commercial viability of existing processes, it would be highly valuable to leverage the usage of ABE as a direct biofuel, while retaining the advantageous characteristics of butanol. Several studies in the past have shown the implementation of ABE in IC engine applications with favorable results in terms of heat-release, main combustion process and emissions. Most notably, engine studies involving ABE/diesel blends demonstrated reduced soot emission output with improved engine efficiency at the expense of increased NO_x emissions [10]. Despite these favorable results, the practicality of ABE has been met with some concerns due the acetone component. Acetone is corrosive towards plastic and rubber components, but also has a very low flash point, which can pose as a safety issue while transporting and storing.

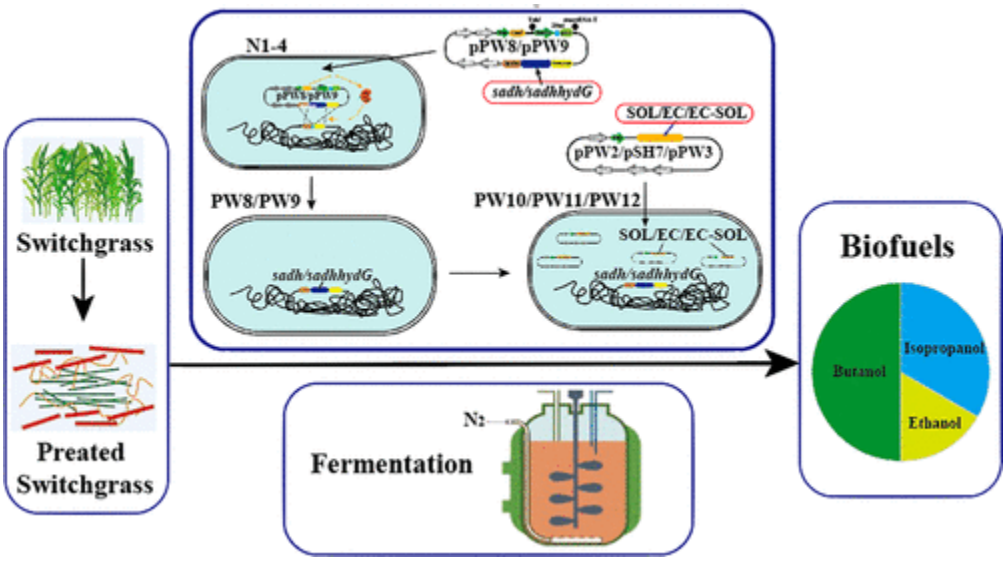

Figure 3: Metabolically engineered Clostridium saccharoperbutylacetonicum via plasmid-based or CRISPR-Cas-9 chromosomal integration. Adapted from [11]

To address the shortfalls of ABE, there has been considerable interest in promoting the "acetone-to-isopropanol" pathway in ABE-producing strains to produce isopropanol-butanol-ethanol (IBE) mixtures. Unlike acetone, isopropanol has a higher energy density (23.9 MJ/L vs 22.6 MJ/L) with a considerable higher flash point (-17^{o}C vs. 12^{o}C) that will likely experience lower degradation issues. Moreover, the attractiveness of IBE has been further strengthened due to recent advances in metabolic engineering. Wang et al. have demonstrated that ABE producing c*olstridium saccharoperbutylacetonicum* can be genetically modified via plasmid-based or CRIPR-Cas9 chromosomal-integration methods to effectively produce IBE [11] as seen in ***Figure 3***. The resultant engineered strain has proven to produce the highest reported yield of IBE from acetic-acid-pretreated switch grass biomass in a batch fermentation process.

To date, limited engine specific studies have been performed on the emission characteristics of IBE when blended with commercial diesel. In these studies, the change in emission level of IBE-diesel blend was measured by 1) increasing the volumetric percentage of

IBE in the IBE-diesel blend, 2) changing the component ratio of IBE, and 3) by employing exhaust gas recirculation (EGR) technique with a dilute gas in the engine. While all these studies show favorable emission characteristic of IBE, they fail to decouple the effect of fuel structure from that of engine technology and operating conditions. Moreover, although the soot reducing potential of IBE has been clearly demonstrated in the past studies, a fundamental understanding of the soot reducing mechanism from a reaction kinetics perspective remains unclear.

1.2. Objectives

The objectives of this thesis were:

- To design, develop and characterize an experimental apparatus to perform fundamental studies of the sooting tendencies of oxygenated fuels. A laminar, co-flow diffusion flame burner was developed, where soot measurements were performed by implementing color ratio pyrometry technique utilizing a simple and inexpensive consumer grade digital camera. Sooting tendency of measured fuels is reported in terms of the Yield Soot Index (YSI). The motivations behind adopting the YSI method (explained in section 2.2.5) are to unify the present results on a universal sooting scale to compare with past reported YSI of other fuels, its lower overall uncertainty, its requirement of very little liquid fuel for analysis, and most importantly its suitability to conduct soot measurements solely based on fuel chemistry. The details of the entire experimental methodology are given in Chapter 3.
- To examine the soot reducing potential of IBE when added to diesel. For this study, a surrogate diesel was adopted to decouple the chemical complexity associated with commercial diesel and was composed of 70% n-decane and 30% 1-methylnaphthalene by volume.

- To examine the individual effect of carbon and oxygen loading of IBE on its sooting tendency. For this study, the original IBE composition was modified by varying the volumetric ratios of butanol and ethanol in the IBE mixture.
- To examine the soot reducting effect of CO_2 on IBE. CO_2 is a major proponent of exhaust gas recirculation, a common emission reducing technique implemented in practical applications.
- Elucidate fundamental insight to the reaction kinetics contributing to soot formation in IBE, and IBE blended mixtures. Numerical studies were performed by simulating laminar 2D co-flow diffusion flames using laminarSMOKE++, a CFD flame solver and a comprehensive high-temperature C_1-C_{16} kinetic mechanism.

CHAPTER 2: LITERATURE REVIEW

2.1. Historical overview of biofuels

The history of biofuels dates back to 1930s when G. Chavanne of the University of Brussels in Belgium invented a process to transform vegetable oils to fuels [12]. Since then, several types of biofuels have been introduced as alternatives to petroleum derived fuels for combustion applications. To date, four different generations of biofuels exist and have been categorized based on the sources of their production (see ***Figure 4***).

First-generation biofuels are obtained from food crops such as corn, sugarcane, and vegetable oil through yeast fermentation of the crops' sugar or starch content. Bioethanol and biodiesel (fatty acid methyl ester) are common examples of first-generation biofuels. While food crops grown for producing first-generation biofuels lower greenhouse gas (GHG) emissions by capturing atmospheric CO_2, their production and transportation at the same time contribute to higher emissions compared to those of fossil fuels, thus having a positive net GHG life cycle cost. Additionally, since their energy density is lower compared to that of fossil fuels, they need to be produced on a large-scale and hence require vast amount of arable land, water, and fertilizers. This not only drives the prices of food crops high but also harms biodiversity by increasing deforestation for additional land.

To alleviate food supply crisis, second generation biofuels were introduced which are produced from non-food energy crops such as switchgrass, jatropha, whole crop maize etc. and biomass residue such as stem, leaves and husks. Energy crops can be grown on marginal land and hence do not divert land resources required for growing food crops. In addition, most of these energy crops

are perennial in nature and hence need not be replanted as frequently as food crops. However, second-generation biomasses have their own set of shortcomings. For instance, the processing technology to derive fuel from energy crops is different from that for food crops and is not well established. Also, the heavier weight of these crops makes their transportation and handling more difficult. Finally, second-generation fuels do not fully address the food vs fuel debate as the energy crops compete for the same agricultural and labor input as food crops.

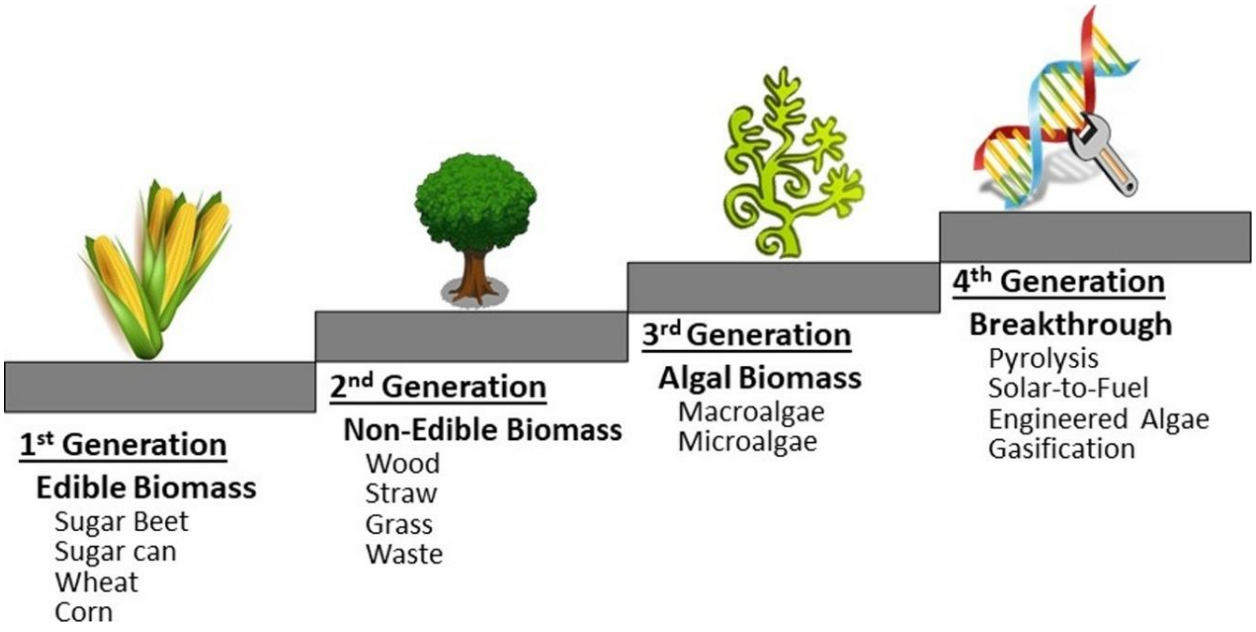

Figure 4: First, second, third and fourth generations of biofuel. Adapted from [13]

Third-generation biofuels are derived from algal biomass such as microalgae, macroalgae, and cyanobacteria. Unlike both first and second-generation biomasses, algae require minimal land use as they can be grown in ponds, lakes, oceans, and waterfalls. They can even be grown on wastewater and provide two-fold benefit by removing nitrogen and phosphorous. Major advantages algal biofuels possess over the previous generation biofuels are that they have higher energy yield, produces less amount of carbon monoxide and almost no amount of nitrous and sulfur oxides. However, these fuels have their own share of shortcomings. One of the major

disadvantages of algae fuel is its high production costs. Algae plantation is highly water-intensive. For instance, 1 litre of microalgae-based biodiesel production requires between 607 and 1944 litres of water [14]. Additionally, algae cultivation demands nutrient input such as phosphorus, which is a scarce resource, thus driving the cost of production higher. According to a 2010 study, algal oil production cost ranged from $10.87/gallon to $13.32/gallon [15]. This is significantly higher than crude oil production and hence its commercialization is not economically viable. Apart from economic standpoint, algal fuel also has physical disadvantage. For instance, microalgae-based biodiesel tends to crystallize under extremely cold temperatures and hence needs to be mixed with regular diesel.

Recent scientific advances have enabled to genetically modify algae biomass to enhance biofuel production. Hence, fuels derived from genetically modified algae are categorized as fourth generation biofuels. Strategies employed in genetic modification involve improving photosynthetic efficiency, increasing light penetration, and reducing photoinhibition [16]. In addition, metabolic engineering of microalgae can increase its content of lipid and carbohydrate, which are essential materials for biodiesel and bioethanol production respectively [17]. However, genetically modified algae pose great health and environmental risks and hence their cultivation needs to be strictly regulated. Some of the health risks associated with exposure to genetically modified algae are toxigenicity and allergenic responses [18]. On the other hand, the potential environmental concerns are competition with native species and changes in natural habitats. Genetic modification of algae enables them to grow faster and withstand harsh environmental conditions. Hence, they are largely capable of invading and surviving in native communities.

Since each generation of biofuel has advantages and disadvantages, it is unclear as to which amongst the four generations is the most favorable alternative to fossil fuels in the future. In

addition, the advent of fracking and other advanced technologies have led to the increase in supply of crude oil while reducing its price. Hence, in the absence of government's intervention in mandating use of biofuels or imposing heavy tax on carbon emissions, sustainability of biofuels for meeting energy demands can be ensured only if their production can be commericialized.

2.2. Background of Sooting Index

A sooting index is a metric to quantify the sooting propensity of one fuel compared to the other in a specific experimental configuration. There are currently several sooting indices present in the literature and each will be summarized in the upcoming sub-sections.

2.2.1 Threshold Sooting Index

Calcote and Manos [19] introduced the concept of threshold sooting index (TSI) to rank the sooting tendency of pure hydrocarbon fuels. It is based on the concept of smoke point, which is the maximum height of a non-smoking flame in a test lamp fueled by the compound of interest. The TSI of a compound or a fuel is defined as

$$\mathrm{TSI} = \mathrm{a}\left(\frac{\mathrm{MW}}{h}\right) + \mathrm{b} \tag{2.1}$$

where a and b are constants and depend on the experimental apparatus, MW is the molecular weight, and h is the smoke point of the fuel. Since the values for a and b differ with respect to the experimental apparatus used for smoke point measurement, they allow for scaling and thus make TSI experiment independent. Ethane and methylnaphthalene are assigned a nominal TSI value of 0 and 100 respectively to set a scale for the remaining compounds. **Figure *5*** shows the TSI measurements for several hydrocarbon fuels performed by Calcote and Manos in diffusion flames.

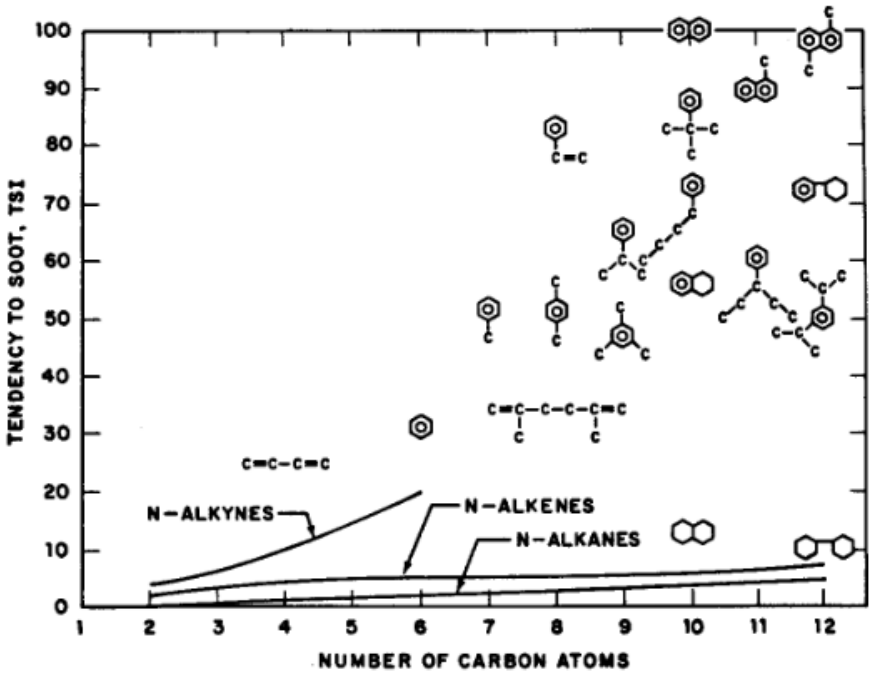

Figure 5: TSI measurements as a function of carbon number and molecular structure. Referenced from [19]

2.2.2 Oxygen Extended Sooting Index

Although TSI measurement has been performed in the past to determine the sooting tendency of several compounds, it is ineffective in the case of oxygenated fuels. This is because molecular weight of a fuel used in TSI is not proportional to the volumetric stoichiometric air requirement of the flame when oxygen atoms are present in the fuel. Hence, Barrientos et. al [20] defined a new sooting index called Oxygen Extended Sooting Index (OESI). For a general fuel with the formula $C_nH_mO_p$, OESI is defined as

$$\mathrm{OESI} = a\left(\frac{n + \frac{m}{4} - \frac{p}{2}}{SP}\right) + b \tag{2.2}$$

where a and b are constants dependent on the experimental setup and SP is the smoke point of the fuel. OESI ranks fuels on a scale from 0 to 100 with 0 being the least sooting tendency value.

2.2.3 Fuel Equivalent Sooting Index

Lemaire et al. [21] introduced a new sooting index called Fuel Equivalent Sooting Index (FESI) which is based on the measurement of peak soot concentration in a turbulent spray flame. Spray flame was chosen for getting experimental data as it closely resembles practical combustion systems.

2.2.4 Micropyrolysis Index

Since soot measurement of a fuel depends on experimental conditions such as flame temperature and stoichiometric oxygen/fuel ratio, Crossley et al. [22] proposed a new sooting index called Micropyrolysis Index (MPI) which quantifies sooting tendency of a fuel without being affected by the above operating conditions. MPI measurements are conducted by pyrolyzing 20 μL of fuel across a bed of α-Al_2O_3 beads at 850 °C temperature. The carbon which gets deposited on the α-Al_2O_3 beads during pyrolysis are then burned in a reactor via temperature programmed oxidation and subsequently the amount of carbon deposited is measured. This amount correlates to the sooting tendency of the fuel being analysed. N-octane and decalin are the reference fuels and are assigned MPI values of 5 and 20 respectively. Good agreement is found between the MPI and TSI values of pure nonaromatic hydrocarbons.

2.2.5 Yield Sooting Index (YSI)

Since user bias exists while measuring the smoke point, which is the sole basis on which a TSI value is given to the fuel, TSI is considered to vary significantly from one experiment set to another. Moreover, TSI measurements are ineffective for highly sooty compounds such as

aromatics because of their negligible smoke point, which is difficult for the user to measure. To address the inadequacy of TSI measurement in terms of accuracy and precision, a novel sooting index called Yield Sooting Index (YSI) was proposed by McEnally et al [23]. YSI measurement involves doping a co-flowing methane-air laminar diffusion flame with the fuel of interest in a very small concentration. Fuels (also called dopant) can be added to the methane-air stream either by mass fraction or mole fraction. Since the molecular weight of a real fuel is unknown, it can be added on mole fraction basis. While all the studied dopants in this research work were either pure compounds or surrogate fuels, they were added on the basis of mass fraction so that their YSI values could be easily compared to those of real fuels measured in the future.

YSI measurements are experimentally independent since they are based on the maximum radially integrated soot volume fraction, $F_{v,max}$ in a laminar diffusion flame. Radially integrated soot volume fraction, $F_v(z)$ can be calculated from a 2D soot map obtained from raw light intensity data in this work and is defined as

$$F_v(z) = \frac{1}{\pi R^2} \int_0^R 2\pi r f_v(r,z) dr \tag{2.3}$$

where R = 6 mm and is the outermost edge of the flame where soot formation has been accounted for [24]. With the above information from the experiment, YSI can be defined as

$$YSI = (YSI_A - YSI_B) * \frac{F_{v,max} - F_{v,max,B}}{F_{v,max,A} - F_{v,max,B}} + YSI_B \tag{2.4}$$

where *A* and *B* represent the reference compounds which in our case are hexane and benzene and their YSI values are 0 and 100 respectively. A more simplified version of the above equation is the following

$$YSI = \alpha * F_{v,max} + \beta \quad (2.5)$$

where α and β are constants and depend on the specific experimental apparatus.

Several diagnostic methods such as Laser Induced Incandescence (LII) and Color Ratio Pyrometry (CRP) have been used in the past to perform YSI measurements of pure compounds and fuels. However, CRP was the preferred method for this work because of its inexpensive nature and ease of use. The method will be described later in Chapter 3.

2.3. Previous soot studies of oxygenated and non-oxygenated hydrocarbon fuels

2.3.1. Laboratory scale flame studies

Several experimental soot studies of both oxygenated and non-oxygenated hydrocarbons have been performed in the past in laboratory-scale flames. For instance, McEnally et al. measured the sooting tendency of a total of 275 compounds including alcohols, ethers, aldehydes, ketones, esters, alkanes, alkenes, and cycloalkanes in a non-premixed methane flame [25]. The soot concentration in these flames were measured in terms of Yield Sooting Index (YSI) with Laser-Induced Incandescence (LII). Results showed that compounds with higher carbon number exhibited higher sooting tendency. Comparing oxygenated and regular hydrocarbons with same number of carbon atoms showed that the former were not always more effective in suppressing soot. For instance, **Figure *6*** compares YSI values of several alkanes and linear chain alcohols and ethers at same carbon number and shows that YSI increases in the following order: ethers <1-alcohols ≈ n-alkanes < secondary alcohols.

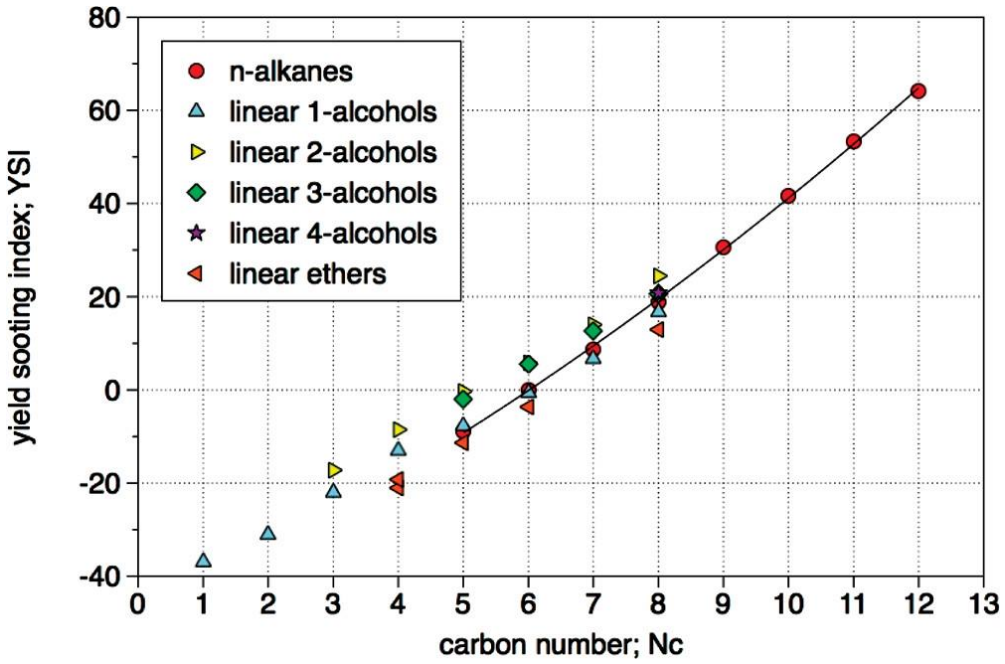

Figure 6: Measured YSI values of n-alkanes, alcohols and ethers as a function of carbon number [25]

Das et al. measured the YSI values of commercial as well as surrogate diesel and jet fuels using a similar approach as McEnally et al [24]. However, the optical diagnostic method utilized in this study was color-ratio pyrometry. It was concluded that the surrogate mixtures were able to replicate the sooting behaviour of the target fuels.

Allan et al. performed smoke point tests on candles made from different primary alcohols (octadecanol, docosanol, hexadecanol) and carboxylic acids (stearic, palmitic, lauric, myristic) [26]. While smoke points for primary alcohols decreased with increasing C/H ratio, the same relation could not be inferred for carboxylic acids.

In addition to individual fuels, soot measurements have also been performed on flames of fuel mixtures containing both oxygenated and petroleum derived fuels such as gasoline and diesel. For instance, Lemaire et al. studied the effect of ethanol on soot formation in turbulent spray flames

fueled by ethanol/gasoline and ethanol/surrogate gasoline blends [27]. Threshold Sooting Index (TSI) values for these blends were obtained from soot volume fraction measurements by coupling Laser-Induced Incandescene (LII) with Laser-Induced Flourescence (LIF). It was found that ethanol addition to both commercial as well as surrogate gasoline led to reduction in soot formation. This was due to reduction in C/O ratio as well as increased CO formation which removed carbon from soot participation.

Gao at al. studied the effect of dibutyl ether (DBE) addition in biodiesel surrogate (methyl decanoate) on soot formation [28]. Mole fractions of dibutyl ether in the fuel stream varied from 0 to 40 mol%. Two-dimensional soot volume fraction profile in a laminar co-flow diffusion flame was obtained with LII technique. The DBE addition was found to lower soot loading in the flame and the soot reduction effect was non-linear with increasing DBE mole fraction.

Chen et al. studied the effect of addition of four butanol isomers (normal, secondary, iso and tertiary butanol) in partially premixed flames of diesel surrogate (80% n-heptane and 20% toluene in volume) [29]. The isomers were mixed at volumetric fractions of 20% and 40%. LII and LIF techniques were employed to measure PAH concentration and soot volume fraction. Results showed that addition of all the four butanol isomers led to soot reduction in the flame. Reduction in toluene content due to butanol addition was deemed to be the dominant factor for soot reduction. Moreover, branched carbon chain butanols (tertiary and isobutanol) were less effective in soot reduction compared to straight chain butanols (normal and secondary butanol) as the former produced more propargyl radicals.

Tran et al. performed smoke point tests and soot volume fraction measurements using LII technique for fuel mixture of soybean biofuel and ultra-low sulfur diesel [30]. The volumetric fraction of the biofuel varied from 0 to 25%. Results showed that fuel mixtures with greater biofuel

concentration smoked at greater flame heights and hence proved that biofuel addition indeed aids in soot reduction. Soot volume fraction measurement was the highest for B0 (pure diesel) and the lowest for B25 (25% biofuel in diesel).

2.3.2. Numerical studies

Several numerical models have been developed in the past to characterize fuel decomposition, and PAH and soot formation for various oxygenated as well as non-oxygenated hydrocarbons. At the same time, these models have been extensively benchmarked against experimental data in various types of combustion studying devices.

Cuoci et al. conducted a detailed kinetic modeling study of PAH formation in co-flow methane diffusion flames with various dilution levels of nitrogen [31]. The flames were simulated using laminarSMOKE++, a CFD solver based on OpenFOAM. Both experimentally and numerically, it was found that diluting the methane fuel stream with nitrogen led to reduction in PAH formation. Simulations also allowed to interpret the data by showing reduced concentrations of C_3 and C_4 hydrocarbons which are important intermediates for benzene formation.

Cheng et al. simulated soot volume fractions and analyzed the reaction pathway for PAH formation in methane co-flow diffusion flames doped with alkylbenzene isomers [32]. The mechanism used in this study was a combination of fuel oxidation and soot mechanisms. Simulations were performed in CHEMKIN's closed homogeneous reactor model. Soot volume fraction was correlated to the mass fraction of a pseudo specie (BIN13A) in the soot mechanism and showed good agreement with the experimentally measured data. Reaction pathway analysis showed that alkylbenzenes do not follow the traditional route, which is hydrogen abstraction carbon addition (HACA) [33], to form PAH. Instead, they tend to combine with each other to generate pyrene.

Liu et al. [34] studied soot formation in methanol-gasoline co-flow diffusion flames using CHEMKIN's 0-D constant pressure model. Toluene reference fuel (TRF) PAH mechanism including n-heptane, iso-octane, and toluene was utilized to model gasoline and hence combined with methanol mechanism to perform reaction pathway analysis in this study. The observed soot reduction effect of methanol addition was attributed to the dilution of aromatics content in the fuel mixture.

Similar study was performed by Gao et al. [28] on addition of dibutyl ether (DBE) in biodiesel surrogate (methyl decanoate). Simulations were performed by applying the opposed flow flame model from CHEMKIN and a reduced mechanism with reactions for both methyl decanoate and dibutyl ether was used to perform reaction pathway analysis for PAH formation in the flame. Results showed reduced concentrations of benzene and pyrene whereas acetylene concentration increased with DBE addition to biodiesel surrogate. The increased acetylene concentration thus promoted soot surface growth process in the annular region of the flame via HACA mechanism whereas had a little role to play in the soot size growth in the flame centerline. On the other hand, the reduced benzene and pyrene concentrations led to soot growth suppression. DBE addition was found to suppress propargyl radical formation and thus the odd carbon reaction pathway which is dominant for benzene formation. In addition, CO formation increased due to the presence of oxygen in its fuel structure, thus preventing carbon from participation in soot formation process.

2.4. Previous studies on the effect of carbon dioxide addition on soot

The effect of carbon dioxide addition on both soot formation and oxidation in hydrocarbon flames has been extensively studied in the past. Experiments have been performed in both premixed and non-premixed flames. In non-premixed flames, experiments have been performed by adding CO_2 on both the fuel and oxidizer side of the burner [35], [36]. Regardless of the type

of flame studied and the location of CO_2 addition, all these studies clearly show soot reduction in the flame. All the premixed flame studies show that CO_2 addition leads to acetylene reduction which subsequently inhibits PAH and soot formation [37], [38]. However, there have been conflicting arguments on the underlying mechanism for soot reduction in diffusion flames.

In 1980, Schug et al. [39]found that CO_2 addition only had thermal effect on soot reduction. On the other hand, Du et al. [36]argued that CO_2 could suppress soot formation chemically. In 2001, Liu et al. [40]studied the effect of CO_2 addition in ethylene diffusion flame and concluded that three effects simultaneously played a role in soot reduction i.e., dilution, thermal and chemical. CO_2 acts chemically by reducing H concentration and increasing OH concentration. According to the study, CO_2 consumes H radicals via R1 to form CO and OH radical. The consumption of H radicals slows the soot growth rate which involves H-abstraction reaction. In addition, the OH radicals formed from R1 subsequently are responsible for oxidative attack of the PAH species and thus delayed soot inception.

$$CO_2 + H = CO + OH \quad \text{(R1)}$$

Reaction R1 was also claimed to be the main chemical reaction in another study conducted by Hoerlle et al [41]. The numerical study was performed in ethylene counter-diffusion flame using the KAUST mechanism. The consumption of H radical in R1 would lead to reduced C_2H_3 as H radical can form C_2H_3 via R2. This would further lead to reduced acetylene (C_2H_2) concentration.

$$C_2H_4 + H = C_2H_3 + H_2 \quad \text{(R2)}$$

$$C_2H_3 (+M) = C_2H_2 + H (+M) \quad \text{(R3)}$$

Moreover, CO_2 addition at the same time can consume activated methylene (CH_2*) via R4. Since both acetylene and activated methylene can react to form propargyl radical via R5, their reduced

concentrations decrease the concentration of propargyl radical. Also, since propargyl radical can self-combine to form benzene, the former's reduced concentration suppresses benzene formation.

$$CO_2 + CH_2* = CH_2O + CO \quad \text{(R4)}$$

$$C_2H_2 + CH_2* = C_3H_3 + H \quad \text{(R5)}$$

The study also claimed that the consumption of H radical in R1 could lead to reduced OH concentration in the sooting region by suppressing reaction rate of R6.

$$H + O_2 = O + OH \quad \text{(R6)}$$

Mahmoud et al. [42] also studied the same flame using the same mechanism as Hoerlle at al. Similar argument was made for lower benzene formation by claiming that CO_2 addition lowers acetylene and activated methylene concentrations via R3 and R4 respectively. The study also points out that CO_2 addition reduces H concentration via R1. However, the reduction in acetylene concentration in R3 was claimed to be as a result of lower flame temperature rather than lower reaction rate of R2. Also, Mahmoud et al. found that the lower H concentration instead affected the PAH growth rate by lowering the H-abstraction rate in the HACA process.

2.5. Background of previous IBE studies

In recent years, several studies have been performed on IBE with respect to its combustion, performance, and emission characteristics. These studies were performed by mixing IBE with either commercial gasoline or diesel and thus directly contributed to real world applications. One of the earliest studies compared pure gasoline with various IBE-gasoline blends (10%, 30% and 60% IBE in gasoline by volume) in a port fuel-injection spark ignition (SI) engine [43]. The IBE mixture was prepared by mixing pure isopropanol, n-butanol, and ethanol in 3:6:1 volume ratio to replicate the composition of the natural fermentation product. While IBE60 resulted in the highest peak cylinder pressure compared to other fuels, IBE30 performed better in terms of brake thermal

efficiency, brake specific fuel consumption, carbon monoxide (CO), unburned hydrocarbons (UHC) and nitrogen oxides (NOx). Lee et al. conducted a comparison study on combustion and emission characteristics of diesel blended with both ABE and IBE in a common-rail single cylinder diesel engine [44]. The study was performed under various main injection timings (MIT) but at equivalent engine load. Comparing ABE20, IBE20 and pure diesel, it was found that the addition ABE and IBE to diesel led to a reduction in the brake thermal efficiency as well as NOx and soot emissions. However, NOx emission slightly increases at above a certain MIT for ABE and IBE mixtures. Hence, with adequate optimization of MIT, blends of both ABE and IBE with diesel proved to be environmentally benign compared to pure diesel. Li et al. [45] studied the effect of adding dilute gas in a diesel engine fueled with pure diesel and two IBE-diesel blends (IBE15 and IBE30) to replicate EGR conditions. Compared to pure diesel, IBE-diesel blend resulted in a slower combustion process. While the brake thermal efficiency was always higher for IBE15 compared to pure diesel, it was lower for IBE30 below a certain flow rate of the dilute gas. However, NOx emission decreased, and soot emission increased for all the fuels. Surprisingly, the increase in soot emission for IBE30 was negligible compared to that for pure diesel and IBE15 which indicated that IBE30 could potentially reduce both NOx and soot emission under certain operating engine conditions. Li et al. [46] also studied the effect of injection strategies including main and pilot injection in the same setup. While the main injection timing was fixed, the pilot injection timing (PIT) varied. The combustion process in the engine was significantly affected with the adoption of double injection strategy because of which a reduction in maximum pressure and heat release rate were observed. Other factors that saw improvement were engine performance and economy. An opposite trend was observed for NOx and soot emission for all the fuels. While at

lower PIT, NOx emission decreased and soot emission increased, the opposite was true at advanced PIT.

In addition to the ones discussed above, few experiments on IBE have been performed in a constant volume chamber setup. This setup was adopted mainly to decouple various factors that affect the combustion process in a real engine. Lee et al. [47], [48] studied IBE-diesel blends (IBE20, IBE40, IBE60, IBE80 and D100) at various temperatures and oxygen concentrations. As more IBE was added to diesel, the spray evaporation increased significantly thus lowering the liquid spray penetration in the chamber. Also, maximum cylinder pressure and heat release rate reduced with IBE addition. Ignition delay was longer for the blend compared to pure diesel at lower temperatures (below 800 K) but the difference reduced significantly as temperature increased. Soot emission was always found to be lower for the blend compared to that for pure diesel.

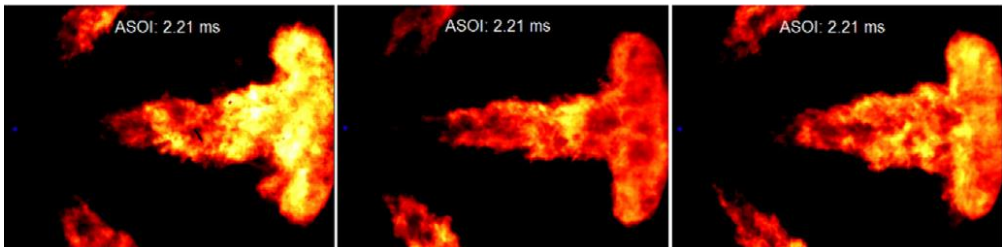

Figure 7: Flame image captured by Lee et al. [48] **in a constant volume chamber for pure diesel (left), IBE20 (center) and IBE40 (right)**

While previously discussed experiments were performed for IBE mixture with 3:6:1 volume ratio, a new study was conducted with a newer volume ratio of 6:3:1 to see the subsequent effect [49]. With more isopropanol in the new IBE mixture, a better spray evaporation and thus shorter liquid spray penetration was observed. The IBE-diesel blends exhibited longer ignition delay but

shorter combustion duration. On the other hand, flame luminosity reduced significantly thus indicating that more isopropanol in the mixture can lead to lower soot emission.

Complementing experimental data, a reduced IBE-diesel mechanism has been introduced recently by Hu et al [50]. It was developed by coupling reduced mechanisms of isopropanol, n-butanol, ethanol, diesel surrogate (n-heptane and toluene) and NOx and soot models and contains 151 species and 775 reactions. Validation against experimental results for laminar speed, ignition delay time and major species profile were performed for individual components to assess the integrity of the sub mechanisms. Furthermore, a 3D engine simulation using KIVA-3V2-CANTERA coupled with the combined mechanism showed good agreement with the experimental results of IBE-diesel blends in terms of cylinder pressure, heat release rate and NOx and soot emission.

2.6. Background of C_1-C_{16} high temperature soot mechanism

The kinetic mechanism used in this work is a combination of gas-phase kinetic model for pyrolysis and oxidation of hydrocarbon and oxygenated fuels, and soot mechanism. This complete kinetic scheme has not only been validated against numerous experimental results to assess its predictive accuracy but also led to the creation of several reduced kinetic schemes for surrogates of transportation fuels (gasoline, diesel and biofuels) [51]. Since n-heptane is usually chosen as a single component surrogate for gasoline, Stagni et al. [52] created a reduced mechanism for n-heptane oxidation and showed good agreement between its prediction of CO and CO_2 formation with measurements in a jet stirred reactor [53]. Similarly, a reduced mechanism created for surrogate diesel containing n-alkanes upto n-hexadecane, toluene, xylene and 1-methylnaphthalene predicted correctly the oxidation of binary diesel surrogate (70% n-decane/30% 1-methylnaphthalene) in a jet stirred reactor at 560 – 1030 K temperature and 10 atm pressure [54]. The earliest validation of the current soot model was through comparison of its

prediction with the experimental data for soot measured in ethylene-argon-oxygen flame in a burner-stabilized premixed flame [55]. The parameters compared were temperature profile, particle size distribution function (PSDF), soot volume fraction and number density for a series of burner to stagnation surface separation distances. While the model was able to reproduce the temperature profile and the progression of particle size distribution (evolution from soot inception to mature stage of size growth), it over predicted soot volume fraction and particle size. Since the experimental boundary conditions were difficult to match exactly, the results were deemed satisfactory. The validation work was pursued further by comparing the soot model's prediction with experimental data collected from 60 rich premixed laminar flames fueled by more than 20 different C1-C10 fuels [56]. The assessment procedure involved comparing concentrations of major species such as CO, CO_2, H_2O, heavier aromatics and PAH and finally soot volume fraction. While overall predictions were found to be reasonable, the slight deviations were attributed to factors such as kinetic model simplification as well as measurement uncertainty in temperature and PAH concentration.

CHAPTER 3: EXPERIMENTAL AND NUMERICAL METHODS

3.1. Co-flow laminar diffusion flame burner and flow conditions

The experimental setup shown in ***Figure 8*** to ***Figure 10*** consists of an atmospheric pressure, laminar diffusion flame burner predicated on the original design developed by Yale. The burner (see **Figure 9**) consists of a 4 mm OD inner fuel tube surrounded by a 74 mm OD oxidizer co-flow tube, where the fuel tube is offset 4 mm higher than the co-flow tube. To ensure uniform oxidizer flow, two Hastelloy-X honeycomb meshes are placed in the annular region of the burner and separated by a cavity filled with 3 mm soda lime glass beads. Downstream of the fuel tube, the fuel stream is prepared by two 500 sccm mass flow controllers (Sierra Instruments), which are calibrated by soap bubble meters. The fuel stream consisted of methane as the base fuel, diluted with nitrogen (both gases >99.9% purity supplied by Airgas). To minimize flame smoking and ensure adequate vaporization of test fuels, the flow rates of methane and nitrogen were held constant at 286 sccm (56.4% mass fraction) and 115 sccm (43.2% mass fraction), respectively. The oxidizer stream is provided to the burner through 4 inlet ports concentrically positioned around the exterior surface of the co-flow tube. Lab supplied compressed air was used as the oxidizer and regulated by a mass flow controller capable of operating up to 75 L/min (Sierra Instruments). The oxidizer flow rate was kept constant at 50 L/min. For EGR relevant experiments, the oxidizer stream was also connected to a mass flow controller (Alicat Scientific) to provide CO_2 (>99.9% purity supplied by Airgas). EGR rate in this study was defined by the CO_2 mass fraction in the oxidizer stream, and hence, experiments were performed for 3% (1017 sccm of CO_2), 6% (2100 sccm of CO_2) and 9% (3254 sccm of CO_2) EGR rates. Beyond these rates soot was undetectable. The accuracy of all mass flow controllers used in this study are ±1.5% of full scale.

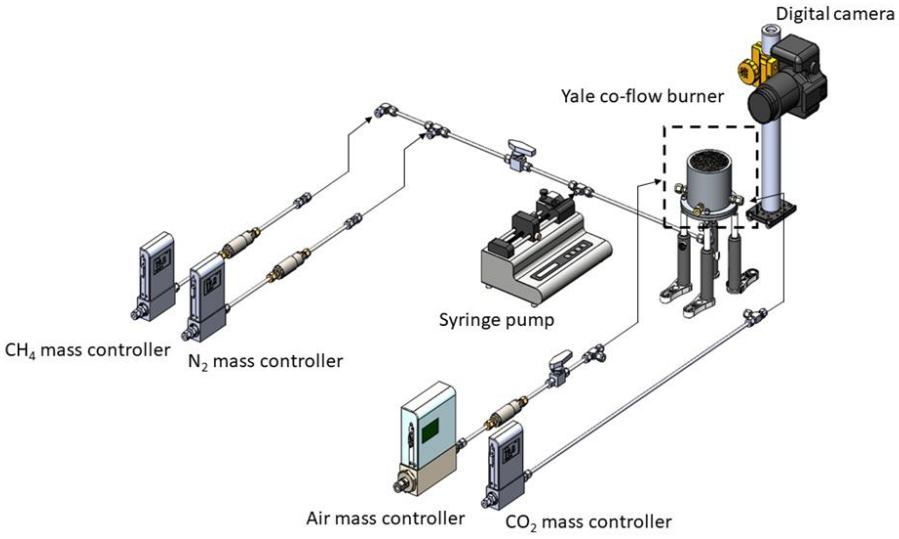

Figure 8: Schematic of the experimental setup

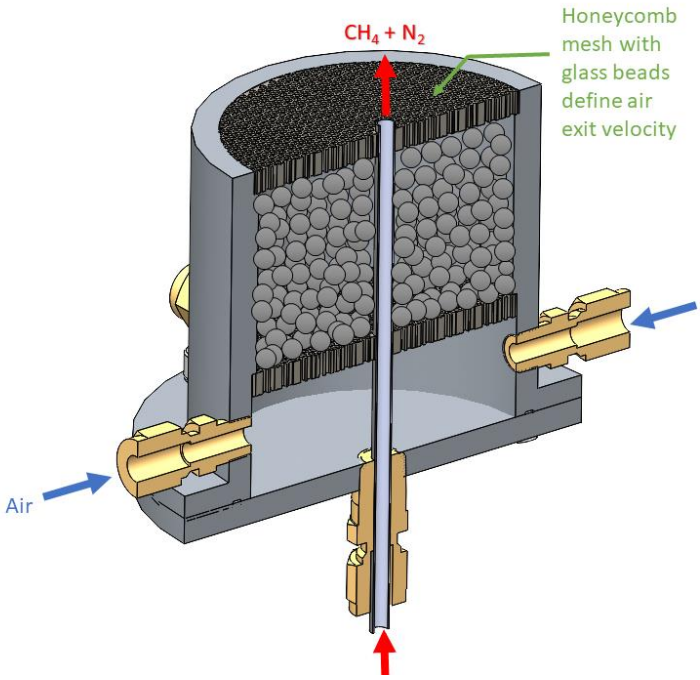

Figure 9: Yale burner sectional view

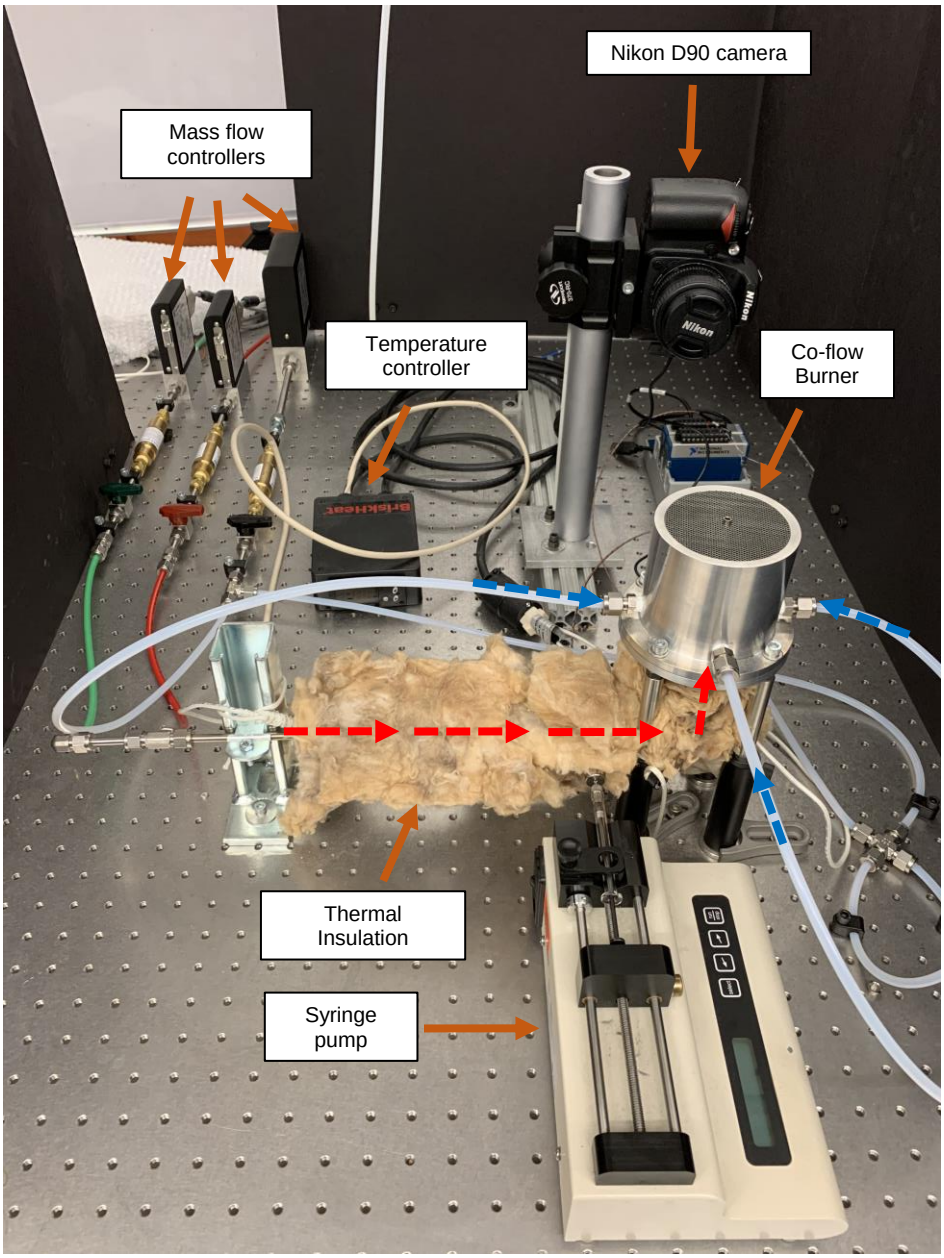

Figure 10: Image of the actual experimental setup. Dashed red and blue lines represent paths of fuel and co-flow air respectively

Test fuels examined in this study where injected into the main fuel stream by a single-syringe infusion pump (Cole Palmer EW-74900), capable of flow rates from 0.200 µL/h to 500 mL/h with an accuracy of ±0.5%. Based on the density of prepared test fuels, volumetric flow rates varied from 98.5 µL/h to 100.2 µL/h to maintain a constant mass fraction of 0.4% of the total fuel

mixture. Test fuels in the liquid phase at room temperature, were vaporized into the fuel stream by heating the main fuel tube above the vaporization temperature of the test fuel using a temperature-controlled heating tape (Briskheat SDCKCA-HTC451005). The gas temperature inside the fuel tube was monitored by a thermocouple (Omega HTTC36-J-14G-1.5-GG) at the location of the septum nut that enables syringe injections into the fuel stream. To minimize heat losses, the fuel tube was wrapped in mineral wool.

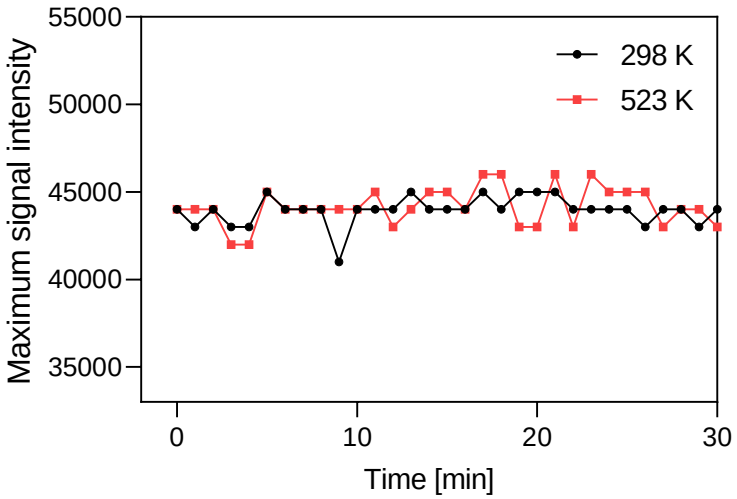

Figure 11: Temporal evolution of undoped methane flame intensity for different fuel tube temperatures

Prior to liquid fuel injection, it was important to determine whether heating the fuel tube and thus changing its temperature had any effect on the undoped methane flame. **Figure *11*** is an illustration of the temporal evolution of methane flame intensity at 298K and 523K inner tube temperatures and clearly shows that flame intensity remains unchanged at 523K. This proves that the change in flame intensity observed in **Figure *12*** is a result of the addition of the liquid fuel only.

An optimal temperature inside the fuel tube for the instant vaporization of all the test fuels was determined by gradually increasing the heating tape temperature and monitoring the signal

intensity of the flame. Complete vaporization of the liquid fuel could be ensured if the signal intensity remained constant over time. An illustration of the process of determining vaporization temperature of IBE0, which is the least volatile fuel blend in this study, is shown in **Figure *12***.

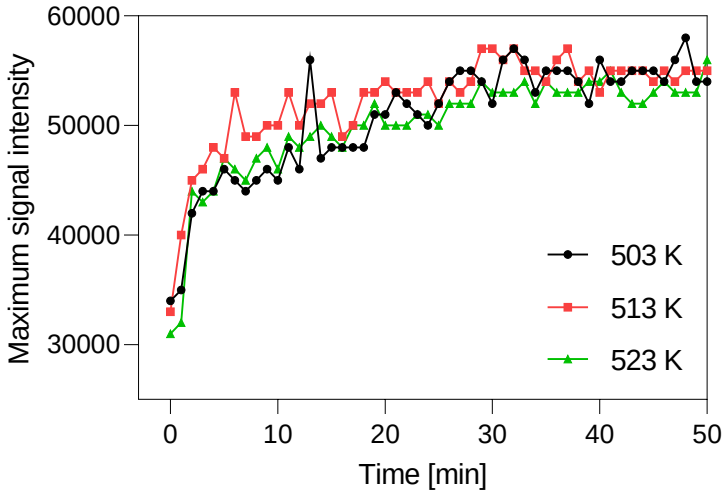

Figure 12: Temporal evolution of IBE0 flame intensity for different fuel tube temperatures

The figure shows the temporal evolution of signal intensity of the flame for three different inner fuel tube temperatures ranging from 503 to 523K. While the signal intensity increased over a period of time after the initiation of fuel injection, it eventually stabilized once the fuel absorption/desorption equilibrium with the inner wall of the fuel tube was attained provided the fuel was completely vaporized. At all the three temperatures, flame intensity stabilized after approximately 40 minutes of fuel injection and hence ensures complete fuel vaporization. Hence flame images were captured only after this stabilization period for soot volume fraction measurement. In addition, while the flame intensities at the initial stage of fuel injection at three temperatures varied, they overlapped after approximately 20 minutes. This proves that flame intensity remains unaffected by increasing the fuel tube temperature from 503K to 523K and that

any one of these temperatures can be safely chosen to conduct the experiments. In this study, the inner fuel tube temperature was maintained at 523K for all the test fuels examined.

IBE mixtures were prepared from pure analytical grade components (Sigma-Aldrich) of iso-propanol (>99.5% purity), n-butanol (>99.4% purity), and ethanol (>99.5% purity) to a volumetric ratio of 0.354:0.491:0.155 to reflect the current IBE mixtures attainable from the engineered strains of Wang et al [11]. To study the individual effect of carbon and oxygen loading of IBE on its sooting tendency (discussed in section 4.2), two additional IBE mixtures (0.354:0.625:0.021 and 0.354:0.021:0.625) were prepared where the volumetric ratios of butanol and ethanol were changed while keeping the ratio of isopropanol constant. Diesel surrogate fuel was prepared similarly from pure analytical grade components (Sigma Aldrich) of n-decane (>99.0% purity) and 1-methylnapthelene (>95% purity) at a volumetric ratio of 70:30. This particular surrogate is chosen in this study due to its wide use as a surrogate in the literature [21], [54], its known ability to share the same physical properties to that of commercial diesel, and its well documented reaction kinetics (see Numerical Methods section). Prepared IBE and diesel surrogate mixtures were mixed to produce IBE-surrogate diesel fuel blends. IBE displayed excellent miscibility with the surrogate diesel components. Fuels blends used in the study varied from 10% to 90% by volume, denoted as IBE10 and IBE90, respectively. Pure diesel surrogate and IBE were also studied, denoted as IBE0 and IBE100, respectively.

3.2. Color ratio pyrometry

Pyrometry is the method of measuring temperature of distant objects with the information of thermal radiation that they emit. It is largely applicable for high temperature measurements where temperature measurement tools such as thermocouple and thermistor fail because of its non-

invasive nature. Color ratio pyrometry determines temperature based on the ratio of signal detected at two different wavelengths with the help of color filters. This method is based on Planck's law equation which is given by:

$$I(\lambda, T) = \varepsilon(\lambda) \frac{2\pi hc^2}{\lambda^5 (e^{\frac{hc}{\lambda kT}} - 1)} \tag{3.1}$$

where $I(\lambda, T)$ is the intensity of radiation emitted by the object at waavelenth λ and temperature T, k is Boltzmann constant, c is speed of light, h is Planck's constant, and $\varepsilon(\lambda)$ is emissivity. Emissivity is the effectiveness of a body to emit thermal radiation and is a function of wavelength and temperature. A blackbody is an ideal emitter whereas all real bodies emit only a fraction of the blackbody's emission at a certain temperature. The monochromatic emissivity of a non-blackbody is defined as

$$\varepsilon_\lambda = \frac{I_\lambda(T)}{I_{b,\lambda}(T)} \tag{3.2}$$

where $I_\lambda(T)$ and $I_{b,\lambda}(T)$ are the emissive power for a non-blackbody and a blackbody respectively at a certain temperature.

The signal S_F detected by any sensor through a color filter is equal to the intensity of radiation integrated over the bandwidth of the filter for a certain time interval τ. Mathematically it is defined as:

$$S_F = (2\pi hc^2)\tau \int_{\lambda_1}^{\lambda_2} \frac{\varepsilon(\lambda)\eta(\lambda)}{\lambda^5 (e^{\frac{hc}{\lambda kT}} - 1)} d\lambda \tag{3.3}$$

where η is the efficiency of the detector over the filter bandwidth (i.e. $\Delta\lambda$). Temperature can be determined by calculating the signal ratio $\frac{S_{F1}}{S_{F2}}$ for a pair of filters F_1 and F_2 as per the following equation:

$$\frac{S_{F1}}{S_{F2}} = \frac{\int \eta_1 \frac{\varepsilon(\lambda)}{\lambda^5(e^{\frac{hc}{\lambda kT}} - 1)} d\lambda}{\int \eta_2 \frac{\varepsilon(\lambda)}{\lambda^5(e^{\frac{hc}{\lambda kT}} - 1)} d\lambda} \tag{3.4}$$

The above equation can then be used to create a lookup table to determine the relationship between signal ratio and temperature of any object. Equation (3.4) can be simplified if we assume that the spectral bandwidth of the filter $\Delta\lambda$ for the two filters is smaller compared to their central wavelength difference. If so, the equation becomes

$$\frac{S_{F1}}{S_{F2}} = \frac{\eta_1 \frac{\varepsilon(\lambda)}{\lambda_1^5(e^{\frac{hc}{\lambda kT}} - 1)} \Delta\lambda_1}{\eta_2 \frac{\varepsilon(\lambda)}{\lambda_2^5(e^{\frac{hc}{\lambda kT}} - 1)} \Delta\lambda_2} \tag{3.5}$$

A color digital camera can be used to implement color ratio pyrometry to measure temperature since it has a filter called Color Filter Array (CFA) placed on top of its image sensor. CFA is a mosaic of tiny color filters and therefore each pixel on the image sensor sees only one color. There are different types of CFAs based on the pattern size and color of the filter. However, the most common type is the Bayer filter pattern (shown in ***Figure 13***), which has a 2x2 pattern with one blue, one red and two green filters and is used in the camera for this work. While each pixel physically only sees a single color, the camera is able to produce a color image by a procedure called demosaicing where the other two color values are interpolated in the pixel based on the

color information from the adjacent pixels. Each camera has its own demosaicing algorithm and thus may produce different image for the same object. Since each pixel can store signal intensity values for all three color channels, temperature of the imaged object can be measured in that pixel by relating it to the signal ratio of any two color channels. For accuracy, all three color channels were utilized to give three signal ratios and thus three different temperatures which were averaged for the final output.

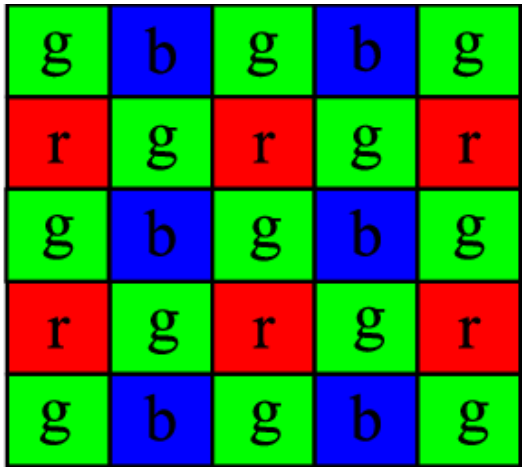

Figure 13: GBRG Bayer pattern in Nikon D90. Adapted from [57]

The filter bandwidth of each color channel in the camera is very broad and overlaps at some wavelengths. Hence, the parameters such as efficiency and emissivity vary widely over a range of wavelengths and hence the simplified assumption of these parameters being constant over the filter bandwidth in Equation (3.5) fails. Instead, the parameters can be integrated over the entire bandwidth of the filter if the spectral dependence of the camera's filter and the emissivity of the imaged object is known. The spectral response of digital cameras (i.e. the efficiency of the camera to detect light at a certain wavelength and factored in the $\eta(\lambda)$ term of Equation (3.4)) are not readily available from the manufacturer and usually needs to be measured in-house. Since a Nikon

D90 camera was used for this study, its spectral response measured by Ma et al. [58] was used as a reference and is shown in ***Figure 14***.

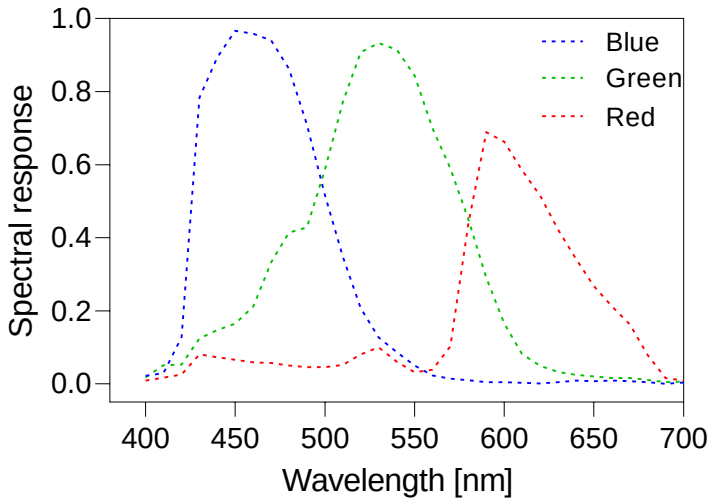

Figure 14: Spectral response curve of Nikon D90 camera. Redrawn from [58]

3.2.1. Camera setup and characterization

A Nikon D90 SLR camera with a NIKKOR 50 mm f/1.4 AF-D lens was used to measure the soot volume fraction in the diffusion flame. The camera has a 12.9 million pixels (2868 x 4352) CMOS imaging sensor and lets the user capture images in 12-bit raw data format. Images were captured in raw format (.nef) as the file contains minimally processed information from the imaging sensor. The raw sensor data was extracted using MATLAB. To do so, the NEF files had to be converted to DNG (Digital Negative) files using Adobe DNG Converter.

All image enhancement settings were set to “none” and “direct sunlight” was selected for white balance. Images were shot at the lowest ISO setting i.e. 200 in order to minimize noise. The shutter speed of the camera was selected such that the signal count for all three-color channels were below the saturation point. Since flame intensity varied for different test fuels, the shutter

speed was adjusted accordingly. A free tethering software, digiCamControl, was used to remotely select camera settings, capture images and transfer them from the camera to the computer.

The camera's sensor was positioned at 33 cm distance away from the flame axis and the aperture was set to f/16 . These configurations were implemented for the validity of parallel ray assumption necessary for Abel inversion (discussed in section 3.2.3) while maintaining high spatial resolution. Since the camera's minimum focusing distance was more than 33 cm, a 14 mm extension ring (Nikon PK-12) was added between the lens and the camera body to capture a focused image.

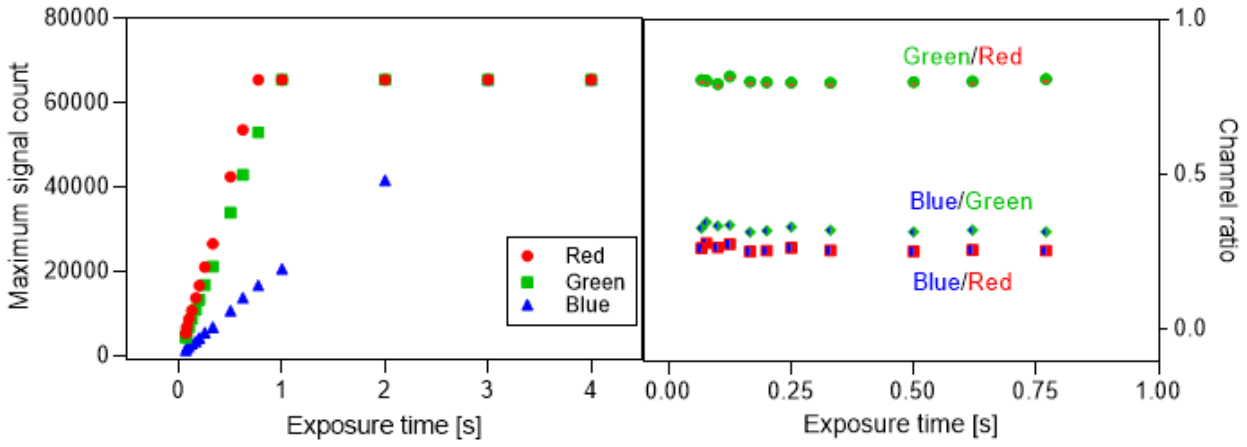

Figure 15: Signal count in the undoped flame centerline as a function of exposure time (left) and linearity region of the camera (right)

To assess the integrity of temperature and soot volume fraction measurement using all three color channels of the camera, it was important to determine each channel's response to a uniform light intensity for various shutter speeds. It can be seen in the left graph of ***Figure 15*** that the signal count for all the three color channels increases linearly with the camera's exposure time until it saturates, thus verifying the camera's performance in detecting light. The right graph of ***Figure 15*** is a further verification of the camera's detection ability by showing constant channel ratios within

this linear regime. While images can be captured at any one of the exposure times within the linear regime, highest signal to noise ratio, which is essential for an accurate temperature and soot volume fraction measurement, can only be obtained at the exposure time just below the saturation point. Hence, all images in this study were captured at the highest possible exposure time.

3.2.2. Calibration using S-type thermocouple

Prior to measuring soot temperature in the flame, it was critical to calibrate the implemented pyrometry technique which required imaging a body with known emissivity and temperature. In this study, a 0.25mm dia. S-type thermocouple (Pt/10%Rh-Pt) was chosen as the calibration source especially due to its suitability for high temperature applications. The calibration was performed by heating the thermocouple above the flame such that it radiated and subsequently capturing its image as seen in **Figure 16** using Nikon D90.

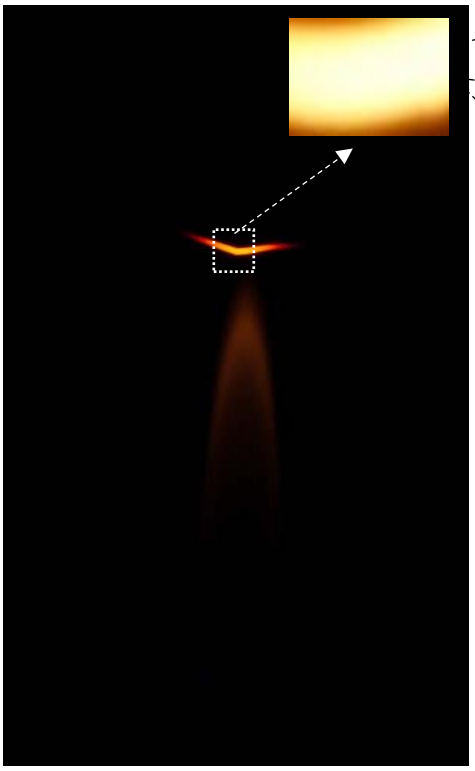

@ 1580K

Red	**30000**
Green	**28000**
Blue	**20000**

Figure 16: Image of the radiating S-type thermocouple. RGB intensity values in the table are given for illustration only

The raw image was converted to TIFF format and its demosaicing was performed in MATLAB. The ouput color image was subsequently split into red, green, and blue channels. Each RGB image was subsequently cropped to include just the thermocouple bead whose temperature could be directly correlated to the self reported thermocouple reading. The cropped region (shown in top right corner of **Figure 16**) was utilized to provide average red, green and blue intensities (shown in the table of **Figure 16**) and thus measure the bead temperature by implementing color ratio pyrometry. The procedure was repeated for a range of thermocouple temperatures to assess the dynamic ability of the camera. The thermocouple temperature was varied by placing it closer to or farther away from the flame. The lowest temperature for evaluating the pyrometry technique was 1400K as the camera was unable to detect the radiation from the thermocouple at temperatures below this value. On the other hand, the thermocouple was heated close to its upper temperature limit which was 1616K.

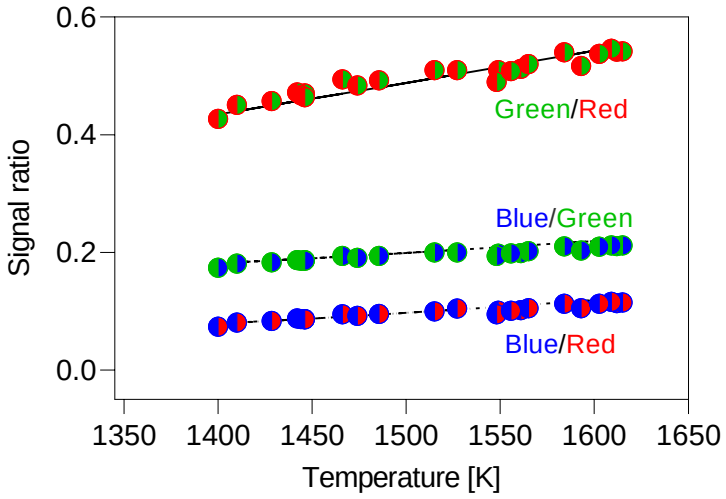

Figure 17: Comparison of calculated (solid line) and measured (points) signal ratio for a range of temperatures for S-type thermocouple

Figure 17 shows the comparison between the calculated and measured signal ratio for this range of temperatures. The theoretical values of three signal ratios were obtained by evaluating the right side of Equation (3.4) where emissivity of the thermocouple was taken as $\varepsilon_L(\lambda) = 1.2018 \times 10^{-6}\lambda^2 - 1.7167 \times 10^{-3}\lambda + 0.9017$ [59].

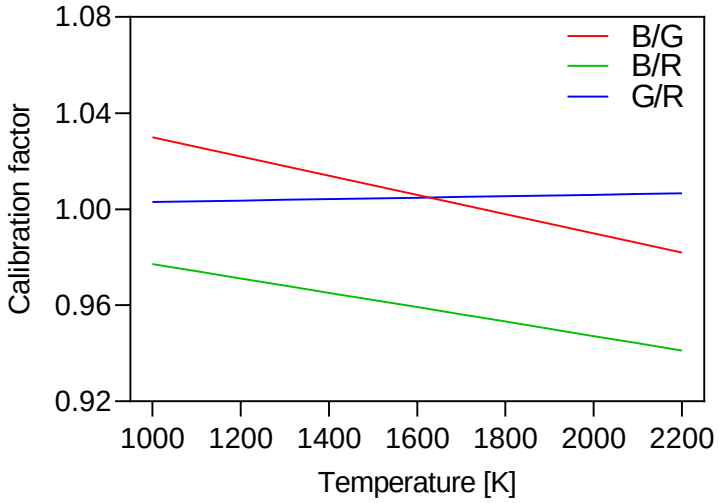

Figure 18: Calibration factor linear fit for three color ratios

Calibration factors for the measured temperature range were obtained by dividing the measured signal ratio from the theoretical signal ratio. Finally, a linear curve fit was applied to the calibration factor as shown in **Figure *18*** and as used to calculate the right side of Equation (3.4) for temperatures ranging from 1000K to 2200K.

3.2.3. Soot volume fraction measurement

Soot volume fraction measurement in typical extinction method such as laser induced incandescence (LII) is based on Beer-Lambert-Bouguer law which relates the ratio of intensity of transmitted and incident light through a flame to the optical depth of soot particles.

$$f_v = -\frac{\lambda}{K_{ext}L}\ln\left(\frac{I}{I_0}\right) \tag{3.6}$$

where f_v is soot volume fraction, λ is the detection wavelength, K_{ext} is dimensionless extinction coefficient (taken as 8.6 in this study, as per the measurements undertaken by Krishnan et al. [60] for soot in the visible wavelength range), L is the characteristic length of the detector (which in this case is the dimension of a pixel of the camera), $\frac{I}{I_0}$ is the ratio of transmitted to incident monochromatic light intensity. The $\ln\left(\frac{I}{I_0}\right)$ on the right side of Equation (3.6) can also be written as:

$$\ln\left(\frac{I}{I_0}\right) = -kl \tag{3.7}$$

where k is extinction coefficient and l is the optical length of soot. Replacing $\ln\left(\frac{I}{I_0}\right)$ term with $-kl$ in Equation (3.6) gives:

$$f_v = \frac{kl}{K_{ext}L/\lambda} \tag{3.8}$$

Since scattering of light by soot particles is ignored under Rayleigh approximation (i.e. size of soot particles is smaller than wavelength of light), extinction is equal to absorption only.

In emission-based diagnostic technique such as color ratio pyrometry, Equation (3.8) is modified by replacing absorption with soot emission by assuming the validity of Kirchhoff's law i.e., at thermal equilibrium, emission is equal to absorption. Hence, soot emissivity, ε, can be defined as:

$$\varepsilon(\lambda, f_v) = 1 - e^{-kl} \tag{3.9}$$

So, Equation (3.8) now becomes:

$$f_v = -\frac{\lambda}{K_{ext}L}\ln[1-\varepsilon] \tag{3.10}$$

As seen in the above equation, determination of soot volume fraction requires soot emissivity measurement, which further requires absolute light calibration at same experimental setup. In this study, S-type thermocouple is used for absolute light calibration due to the availability of its emissivity and temperature values. Soot monochromatic emissivity, ε_S, can be measured by relating soot signal intensity, S_S, at its apparent temperature, T_S, to the calibrated source signal intensity, S_L, at temperature, T_L:

$$\varepsilon_S = \varepsilon_L(\lambda)\frac{\tau_S}{\tau_L}\frac{S_S}{S_L}e^{-\frac{hc}{k\lambda}(\frac{1}{T_L}-\frac{1}{T_S})} \tag{3.11}$$

where τ is an optical parameter of the arrangement used for the flame as well as the S-type thermocouple. Since images of the flame and the S-type thermocouple were taken at the same setup, τ is essentially the exposure time since it was the only parameter changed. As seen in Equation (3.11), soot emissivity calculation requires the knowledge of soot temperature, which was measured by creating a lookup table using Equation (3.5). In the equation, emissivity of soot was approximated as $\lambda^{-1.38}$ with the value of refractive index experimentally determined by Chang and Charalampopoulos [61]. Finally, with all the above information, Equation (3.10) was solved for soot volume fraction.

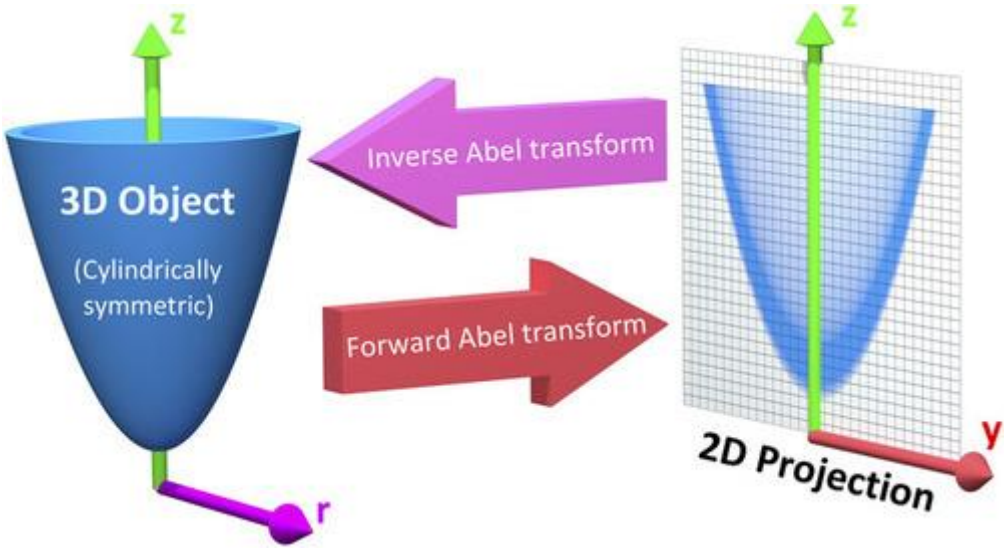

Figure 19: An illustration of Abel transform. Adapted from [62]

The flame image captured by the image sensor of a camera is a 2D projection of the flame since the sensor only measures intensity at its line-of-sight. Since laminar diffusion flames are axisymmetric, the line-of-sight data from their images can be converted to a radial profile by performing tomographic inversion. Among the several techniques that exist, Abel inversion has been used in this study. ***Figure 19*** shows how forward Abel transform can be implemented to construct a 2D projection $P(x,z)$ of the 3D object $I(r,z)$ on a plane (x,z) where x-axis is perpendicular to the z-axis. On the other hand, the inverse Abel transform can be implemented to derive a 3D profile of the flame from its 2D projection on the sensor. Mathematically, the forward Abel transform can be defined as

$$P(x,z) = 2\int_{|x|}^{\infty} \frac{rI(r,z)}{\sqrt{r^2 - x^2}} dr \tag{3.12}$$

The quantity of interest, $I(r,z)$ can be obtained by the following inverse Abel transform equation

$$I(r,z) = -\frac{1}{\pi}\int_{r}^{\infty} \frac{[dP(x,z)/dx]}{\sqrt{x^2 - r^2}}\, dx \tag{3.13}$$

Unfortunately, inverse Abel transform cannot be directly implemented on a flame image as it is impossible to fit a function to a noisy experimental data $P(x,z)$ from the sensor and hence analytically determine its derivative. To address this issue, several numerical methods to evaluate Abel transform of noisy experimental projections have been introduced in the past and one such method is the Basis Set Expansion (BASEX) proposed by Dribinski et. al [63]. This method is based on representing a 3D object as an expansion in a well-behaved set in the (r,z) space and generating the basis in the (x,z) space using Equation (3.12). Any basis set function can be chosen provided it is analytically integrable and is uniform.

An Abel deconvolution is valid only if the incoming rays from the flame to the detector are parallel. On the other hand, practical optical setups collect light rays over a non-zero solid angle. A ray tracing simulation performed by Walsch et al. [64] showed the effect of light collection geometry on Abel inversion error and found that the error diminishes as the ratio of object distance to lens diameter approached infinity while the error being reasonable at ratios over 100. In this study, the optical configuration was chosen such that the ratio was 105 and hence the parallel ray collection in the camera's detector was assumed to be true.

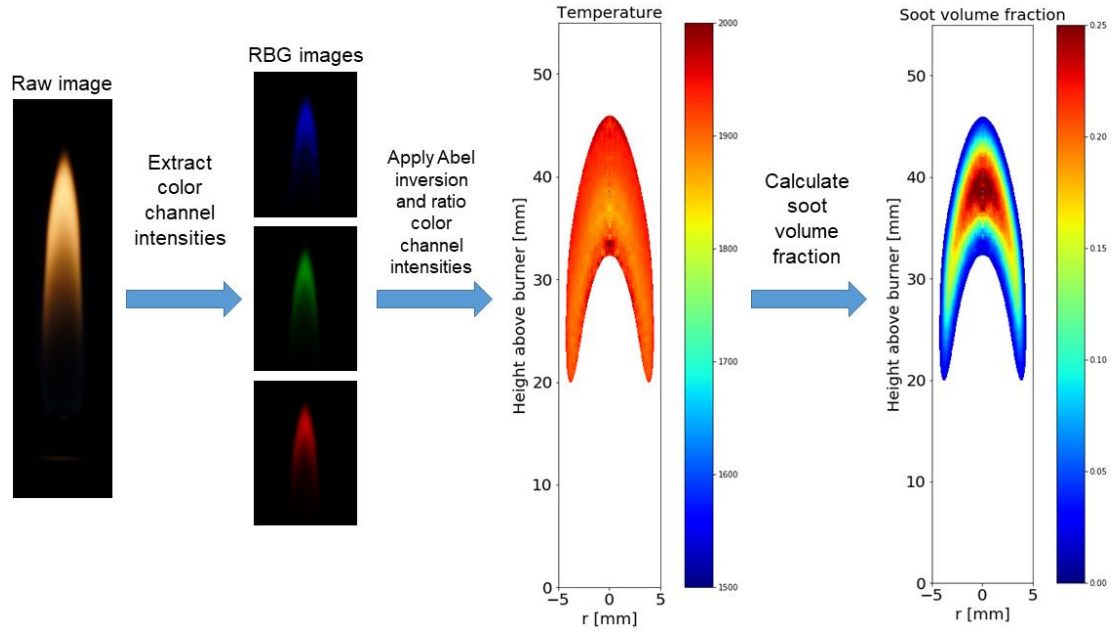

Figure 20: Process flow diagram of soot volume fraction measurement from a flame image

Once the flame image was captured, Abel inversion was applied on each color channel to convert line-of-sight signal intensity to radial intensity. These radial profiles were subsequently divided by each other to give measured signal ratio which was then utilized to calculate soot temperature and soot volume fraction. ***Figure 20*** illustrates post processing steps undertaken to measure soot volume fraction from a flame image.

3.2.4. Experimental validation with previous soot studies

The experimental methodology used in this study was validated by replicating conditions and comparing measuements with those from previous two soot studies in a methane/air diffusion flame. The initial validation was performed in a methane flame studied by Das et al. [65] utilizing color ratio pyrometry in a burner with the exact same dimensions. ***Figure 21***(a) shows a comparison of radially integrated soot volume fraction along the flame height between the two

measurements. In the figure, a deviation in the absolute magnitude of soot volume fraction is observed along the entire flame height. However, it is within an acceptable tolerance with the maximum deviation being 15% and occuring at the peak location of soot in the flame. Also, there is an excellent agreement betweeen the two measurements in terms of locations for soot inception and oxidation.

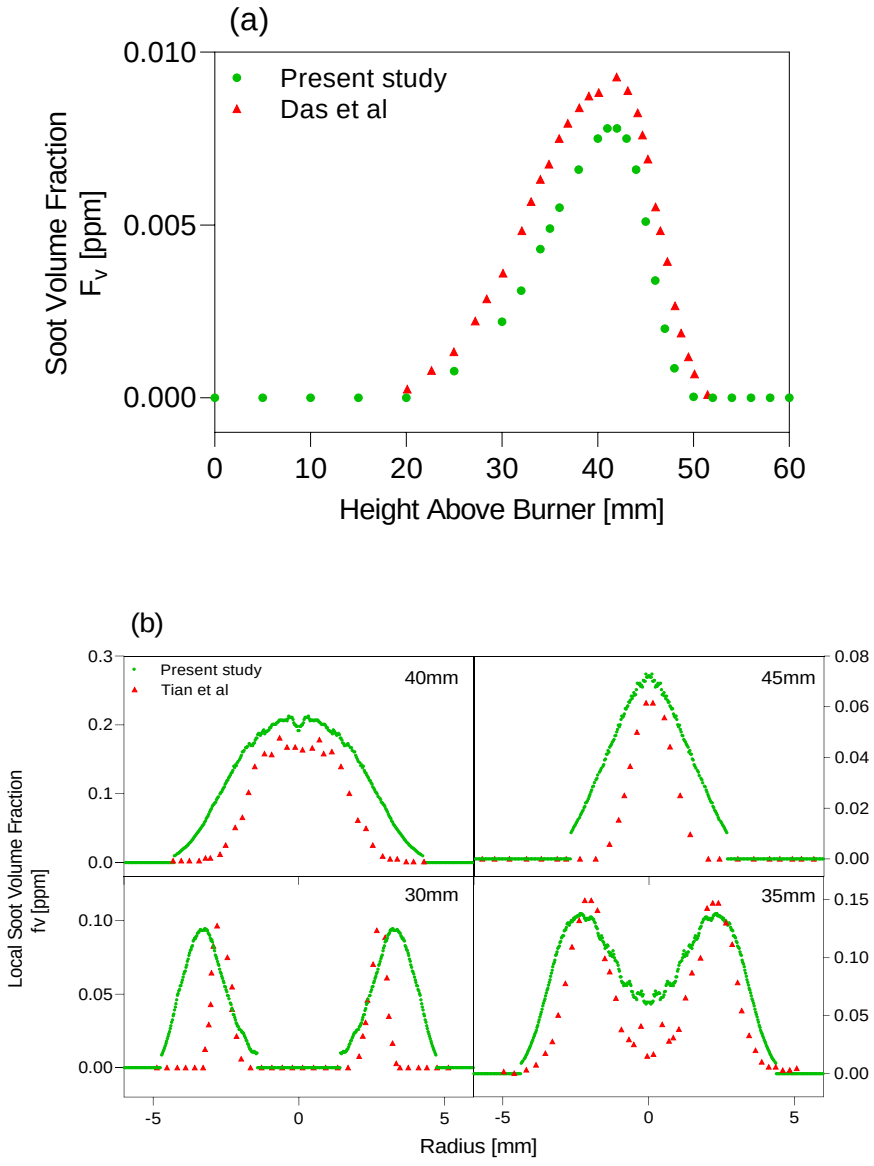

Figure 21: Comparison of soot volume fraction measurement between current study and (a) Das et al. (b) Tian et al.

A second validation was performed by replicating flame conditions studied by Tian et al [66]. Since the burner dimensions were different, the reported flow rates for methane and air were modified to achieve similar equivalence ratio. The reported and modified gas flow rates are presented in ***Table 1***.

Table 1: Burner geometry and flow conditions details

Tien et al.				Present study			
Co-flow tube OD (mm)	**Fuel tube OD (mm)**	**Air flow rate (slpm)**	**CH_4 flow rate (slpm)**	**Co-flow tube OD (mm)**	**Fuel tube OD (mm)**	**Air flow rate (slpm)**	**CH_4 flow rate (slpm)**
96.8	10.5	25.6	0.3	88.9	4.76	20.48	0.240

Figure 21(b) shows the comparison of soot volume fraction radial profile at several heights above the burner exit. It is clearly observed in the figure that the current methodology measures soot at much wider radial locations compared to what has been reported by Tien et al. This discrepancy in radial profiles could possibly be due to the following two reasons: i) variation in flame structure due to the difference in the fuel tube diameter or ii) difference in refractive index used to calculate soot volume fraction. On the positive side, the current experimental methodology is able to replicate the trend in soot evolution radially as well as vertically along the flame.

3.3. Uncertainty analysis

This section discusses the propagation of error due to the uncertainty associated with the parameters that affect soot volume fraction measurement. Equation (3.10) demonstrates that soot volume fraction is a function of soot emissivity, thus suggesting that its uncertainty, U_{f_v} is essentially a function of the uncertainty in soot emissivity, U_{ε_S}. The uncertainty analysis of both

soot emissivity and soot volume fraction have been carried out following the Taylor series method [67]. From Equation (3.11), we know

$$\varepsilon_S = \varepsilon_L \frac{\tau_S}{\tau_L} \frac{S_S}{S_L} e^{-\frac{hc}{k\lambda}\left(\frac{1}{T_L}-\frac{1}{T_S}\right)}$$

On the right side of the above equation, the parameters having uncertainty associated with their measurements are signal intensity from soot, S_s, signal intensity from calibrated light source, S_L, soot temperature, T_S, and calibrated source temperature, T_L. Since soot temperature is related to soot signal intensity, the above equation can be rewritten as:

$$\varepsilon_S = \varepsilon_L \frac{\tau_S}{\tau_L} \frac{S_S}{S_L e^{\frac{hc}{k\lambda T_L}}} \left[\frac{2\pi hc^2 \tau_S \varepsilon_{S,i} \eta}{\lambda^5 S_S} + 1\right] \tag{3.14}$$

where $\varepsilon_{S,i}$ is the estimated soot emissivity required for soot temperature calculation and η is the efficiency of the detector over the filter bandwidth i.e. $\Delta\lambda$. The above equation has been derived by assuming constant emissivity and detector efficiency over the entire filter bandwidth for simplication of analysis. Hence, uncertainty in soot emissivity is given by

$$U_{\varepsilon_S} = \sqrt{\left(\frac{\partial \varepsilon_S}{\partial S_S} U_{S_S}\right)^2 + \left(\frac{\partial \varepsilon_S}{\partial S_L} U_{S_L}\right)^2 + \left(\frac{\partial \varepsilon_S}{\partial T_L} U_{T_L}\right)^2} \tag{3.15}$$

In the above equation, error associated with all the parameters are assumed to be independent of each other and are normally distributed. To calculate U_{ε_S} using Equation (3.15) requires solving the partial derivative of U_{ε_S} with respect to each parameter are given in Equation (3.16):

$$\frac{\partial \varepsilon_S}{\partial S_S} = \varepsilon_L \frac{\tau_S}{\tau_L} \frac{1}{S_L e^{\frac{hc}{k\lambda T_L}}} \tag{3.16a}$$

$$\frac{\partial \varepsilon_S}{\partial S_L} = -\varepsilon_L \frac{\tau_S}{\tau_L} \frac{S_S}{{S_L}^2 e^{\frac{hc}{k\lambda T_L}}} \left[\frac{2\pi hc^2 \tau_S \varepsilon_{S,i} \eta}{\lambda^5 S_S} + 1 \right] \tag{3.16b}$$

$$\frac{\partial \varepsilon_S}{\partial T_L} = \varepsilon_L \frac{\tau_S}{\tau_L} \frac{S_S}{{S_L}^2 e^{\frac{hc}{k\lambda T_L}}} \left[\frac{2\pi hc^2 \tau_S \varepsilon_{S,i} \eta}{\lambda^5 S_S} + 1 \right] \frac{hc}{k\lambda {T_L}^2} \tag{3.16c}$$

Uncertainty in each parameter is calculated in the following manner:

$$U_i = \sqrt{{B_i}^2 + {R_i}^2} \tag{3.17}$$

where B_i and R_i are bias and precision errors respectively. While uncertainty in signal intensity from soot, S_s, and signal intensity from calibrated light source, S_L is due to precision error only, uncertainty in calibrated source temperature, T_L, is due to both bias and precision error. Precision error for all three parameters can be calculated from standard deviation of their measurement. On the other hand, bias error for the calibrated source temperature, T_L, can be obtained from the reported accuracy of the thermocouple (i.e. 1.5^{o}C or 0.25% of the reading, whichever is greater). Once the uncertainty in soot emissivity, U_{ε_S} is obtained using Equation (3.15), it can be used to calculate uncertainty in soot volume fraction, U_{f_v} from the following equation:

$$U_{f_v} = \sqrt{\left(\frac{\partial f_v}{\partial \varepsilon_S} U_{\varepsilon_S} \right)^2} \tag{3.18}$$

where

$$\frac{\partial f_v}{\partial \varepsilon_S} = \frac{\lambda}{K_{ext} L} \frac{1}{\ln[1 - \varepsilon_S]} \tag{3.19}$$

3.4. Numerical method

3.4.1. Numerical solver and simulation setup

The co-flow diffusion flames in this study were simulated using laminarSMOKE++ [68]–[70], a CFD solver for modeling of laminar reactive flows of gas mixtures using a detailed kinetic mechanism. The laminar reactive flows are numerically modelled by conservation equations of mass, momentum, species mass fractions and mixture energy. As per the numerical algorithm of this solver, the conservation equations of mass and momentum are solved by utilizing the PISO algorithm available in OpenFOAM [71], an open-source CFD code. Since detailed kinetic mechanisms includes hundreds of species, this makes the species and energy equations stiff, thus placing a heavy demand on computational resource. To ease computational effort, laminarSMOKE++ implements an operator-splitting technique where the rate of change of mass fractions of species and temperature due to transport processes (i.e. diffusion, convection, heat loss, inflow/outflow etc.) and chemical reactions are calculated separately. The equation below is a general form of transport equation of species and energy following spatial discretization:

$$\frac{d\psi}{dt} = S(\psi) + M(\psi, t) \tag{3.20}$$

where ψ is the vector of mass fractions and temperature, $S(\psi)$ the vector of rate of change of ψ due to chemical reaction and $M(\psi, t)$ the vector of rate of change of ψ due to transport phenomena. Equation (3.20) is solved by discretizing time in the interval of Δt and integrating the equation using the Strang splitting scheme [72].

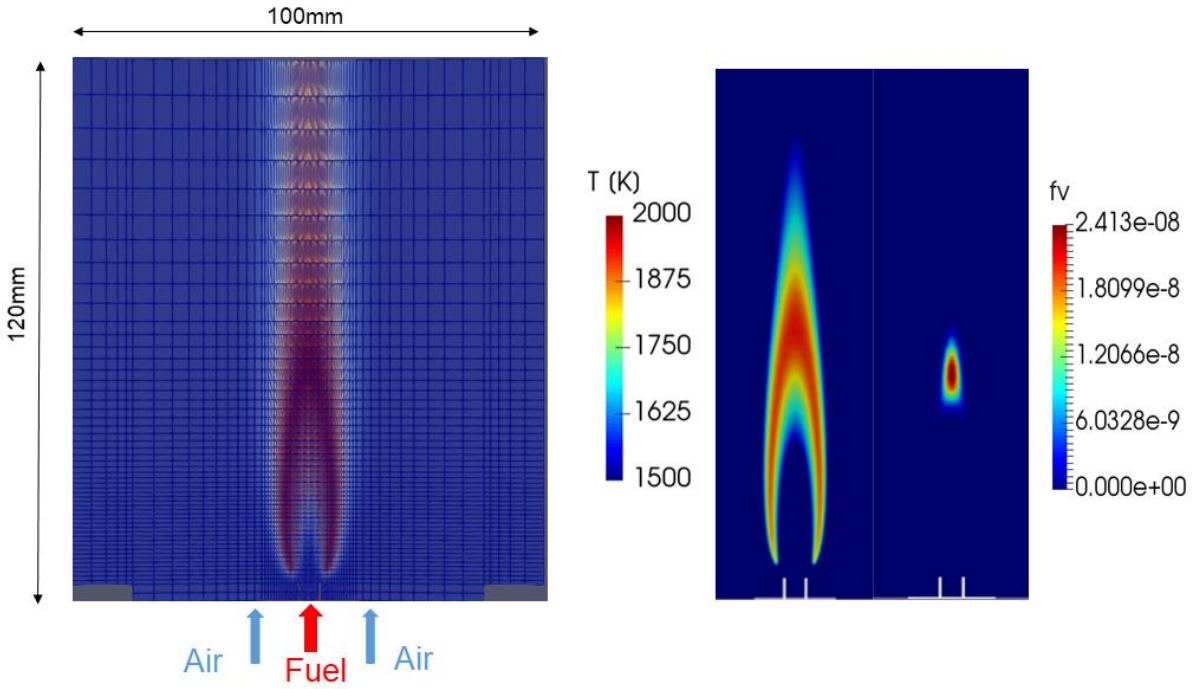

Figure 22: Computational domain (left) and 2D maps of temperature and soot volume fraction (right)

To simulate the experimental flames, a rectangular domain was developed using blockMesh in OpenFOAM with a structured, non-equispaced mesh grid comprising of 60,000 nodes. The rectangular domain was 120mm long and 100mm wide and is shown in ***Figure 22***. Diffusion velocities of species were solved in the model by considering diffusion due to gradient in both species concentration and temperature. On the other hand, radiation effect was neglected in the model, mainly due to the negligible difference in temperature among the undoped and doped flames observed experimentally. For instance, the average flame temperature of the undoped flame, which has the least amount of soot amongst all the studied flames, was measured to be 1970 K. On doping the flame with IBE0, which led to the highest increase in soot formation, the average flame temperature dropped by only 50K. This shows that radiation has minimal effect on flame

temperature, thus validating the assumption of negligible radiation effect in the model. ***Table 2*** summarizes the modeling input parameters used to simulate the experimental flames.

Table 2: Input parameters for simulation setup

Fuel Stream Parameters					**Oxidizer Stream Parameters**				
CO_2 level	**0%**	**3%**	**6%**	**9%**	**CO_2 level**	**0%**	**3%**	**6%**	**9%**
Inlet Velocity	0.785 cm/s	0.68 cm/s	0.55 cm/s	0.49 cm/s	**Inlet Velocity**	0.1945 cm/s	0.1983 cm/s	0.2027 cm/s	0.2072 cm/s
Inlet Temperature	483K	417K	340K	303K	**Inlet Temperature**	300K	300K	300K	300K

3.4.2. Kinetic mechanism

Reaction kinetics and effectively soot formation kinetics within the flame were simulated using a detailed high-temperature C_1-C_{16} chemical mechanism with soot sub-mechanisms developed by the CRECK Melling Group [51], [56], [73]. The soot mechanism is based on a discrete sectional model that categorizes heavy PAHs and soot into 25 different classes of pseudo species (referred to as BIN in the mechanism) based on the number of carbon atoms and thus, can describe the evolution of soot formation from gas-phases species to solid particles. In the mechanism, BIN1 to BIN4 are heavy PAHs with the largest BIN i.e. BIN4 containing 160 carbon atoms and BIN5 to BIN12 are soot particles of spherical shape (particle size ranging from 2.02 nm to 10.11 nm) [74]. Since BIN12 is the largest soot particle, it also acts as a primary building block of the fractal shaped soot aggregates which constitute the remaining BINs i.e. BIN13-25. These species are considered to evaluate soot volume fraction in the model by utilizing a post processing technique incorporated in laminarSMOKE++. Surface growth, nucleation, coagulation, and oxidation processes are also considered in this soot model, where soot surface growth reactions

are described by both the hydrogen abstraction carbon addition (HACA) mechanism and PAH condensation. In total the mechanism contains 452 species and 24,041 reactions, with subsets of chemistry to appropriately describe the kinetics of ethanol, isopropanol, n-butanol, n-decane and 1-methylnaphthalene that are relevant to this study. Although the mechanism has not been previously assessed explicitly against IBE mixtures, it has shown considerably good agreement in prior studies involving the oxidation of 70% n-decane/30% 1-methylnaphthalene surrogate diesel in a jet stirred reactor [54].

3.4.3. Simulation validation

To assess the accuracy of the burner geometry and input parameters utilized for setting up the simulation, it was imperative to see if the simulation captured the main features of the actual flame by comparing its prediction to experimental results. Since flame temperature plays an important role in determining chemical kinetics, it was chosen as the initial parameter for benchmarking the numerical results. ***Figure 23*** shows the comparison between measured and simulated temperature profiles at the centerline of an undoped methane flame at different CO_2 concentrations in the oxidizer stream.

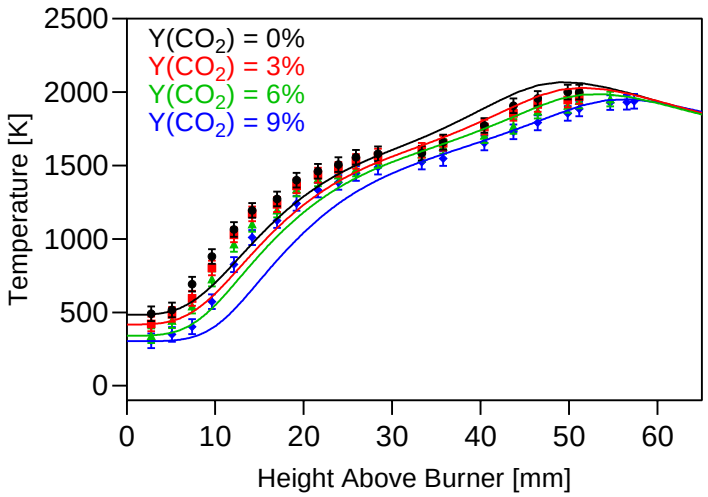

Figure 23: Comparison between centerline temperature of experimental and model flame for a methane diffusion flame

The temperature profile was measured using a S-type thermocouple (Pt/10%Rh-Pt) with a 250 μm wire diameter. The raw thermocouple data was corrected for conduction and radiation losses due to high flame temperature by solving the following equation:

$$T_g = T_j + \frac{\varepsilon_j \delta \left(T_j^4 - T_w^4\right) + \left({}^{2k_j A}/_{l A_{surf}}\right)\frac{dT}{dx}}{{}^{Nu.k}/_{d}} \tag{3.21}$$

where T_g is the gas temperature, T_j is the thermocouple junction temperature, T_W is the ambient temperature, ε_j is the emissivity of the thermocouple junction, δ is the Stefan–Boltzmann constant, d is the diameter of the thermocouple junction (m), A is the wire cross-sectional area, A_{surf} is the surface area of the thermocouple junction, k is the thermal conductivity of the gas, and Nu is the Nusselt number. The thermocouple bead and the adjoining wires were considered to be spherical and cylindrical respectively. The term dT/dx was evaluated by assuming a linear conduction between the bead and the lead wire in the vicinity of the flame wing. As seen in **Figure 23**, simulations are able to replicate the experimental flame heights for an undoped flame at different

CO_2 dilution rates. In addition, the simulation results also show the temperature reduction effect of CO_2 along the entire flame height. In terms of the absolute magnitude of temperature, the experimental and simulation results are in good agreement in the sooting region of the flame. On the other hand, a relatively larger difference is observed between the two in the lower region where conduction loss dominates and can be attributed to the simpler assumption of linear temperature gradient for conduction correction. While a more accurate correction requires calculation of the temperature gradient at each thermocouple radial location through an iterative and thus computationally extensive process, it is clearly beyond the scope of this work and thus was not pursued.

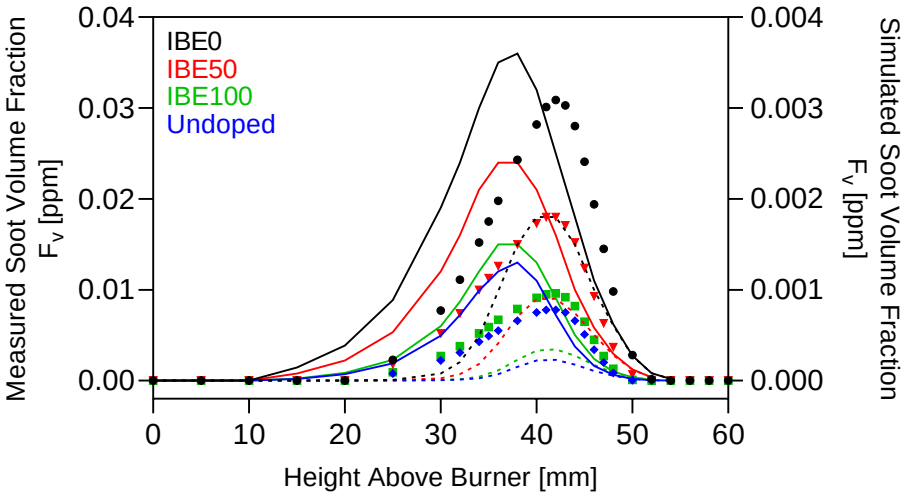

Figure 24: Comparison of radially integrated soot volume fraction between measurement (point) and simulation (solid and dashed line) for IBE0, IBE50, IBE100 and undoped methane flame

Another way to assess the validity of the simulation setup is to compare the residence time for soot in all the simulated flames. ***Figure 24*** shows the comparison between measured and simulated radially integrated soot volume fraction (shown by points and solid line respectively) in both doped and undoped flames. Experimentally, it was observed that soot inception starts at 20mm and

completely oxidizes at approximately 51mm above the burner exit. While the simulation matches the measured location for complete soot oxidation, it predicts premature initiation of soot formation and its peak. This could be due to an indirect comparison of soot between the experiment and the simulation where particle size of soot is unknown in the experiment. To validate this reasoning, simulated soot volume fractions have been calculated for both doped and undoped flames by considering large soot aggregates only and is shown in **Figure *24*** by dotted lines. By doing so, the new peak location for simulated soot volume fraction moves closer to that observed experimentally. On the other hand, simulated soot inception zone is delayed by 6mm. Regardless of what is chosen to calculate soot volume fraction in the simulation, soot residence time is predicted to be unaffected by the concentration of IBE in the fuel blend as soot volume fraction peaks at the same location for all the three doped flames. This is similar to what was observed in the experiment and hence shows that analysis from the simulation is based solely on fuel structure. ***Figure 24*** shows that the simulation underpredicts soot volume fraction for both doped and undoped flames where the maximum deviation is an order of magnitude for IBE0. However, the simulation is clearly able to replicate the trend in soot reduction when more IBE is added to the doped fuel mixture as well as when the flame is undoped. For instance, the peak soot concentration is experimentally observed to reduce by approximately 43% from IBE0 to IBE50 as well as from IBE50 to IBE100, and by only 18.75% from IBE100 to undoped flame. Similarly, the simulation results show that adding 50% IBE in surrogate diesel by volume or that in IBE50 leads to 35% soot reduction. On the other hand, only 13.33% soot reduction is predicted when comparing IBE100 and undoped flame.

CHAPTER 4: RESULTS AND DISCUSSION

4.1. Effect of IBE addition to surrogate diesel

Figure 25 shows measured contour plots of the change in soot volume fraction as the volume percent of IBE is increased in a diesel surrogate mixture. Due to the highly dilute nature of the experimental technique employed, the flame height remained relatively constant at 52 mm regardless of test mixture examined, and indicates that the residence time of chemical reactivity across all flames can be assumed fairly consistent. It can be observed that as the portion of IBE increases, the overall soot formation decreases, demonstrating the soot reducing potential of oxygenated IBE when blended with a hydrocarbon-based fuel. For all the flames, majority of the soot accumulation is observed to be confined within the central region of the flames where it is expected that fuel pyrolysis reactions are dominating.

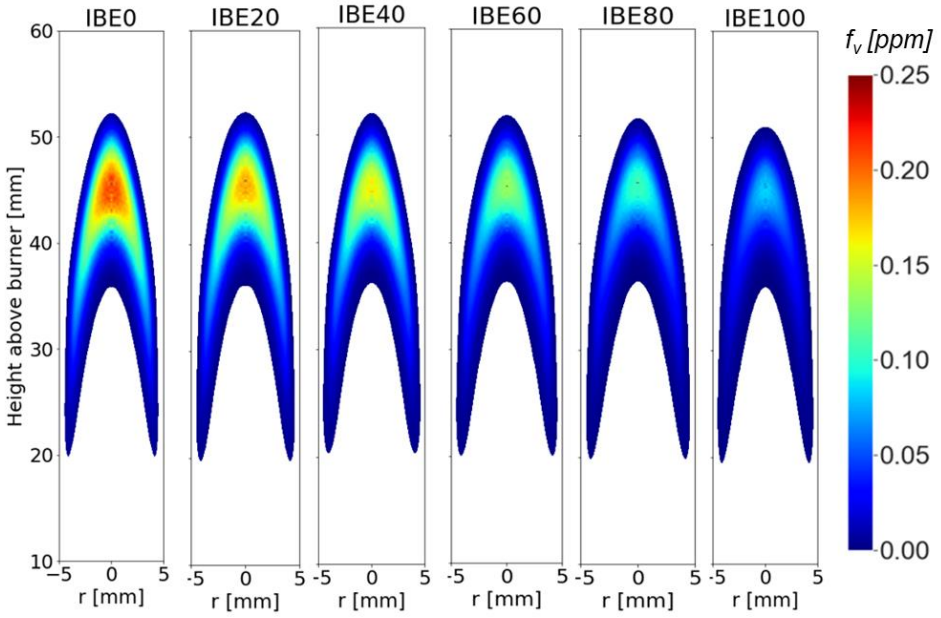

Figure 25: 2D soot volume fraction contour plots for various IBE-diesel surrogate mixture blends

When soot volume fraction is radially integrated across the width of the flame and plotted as function of flame height (see ***Figure 26***), it can be shown that regardless of fuel mixture composition, soot formation begins at approximately 20 mm above the height of burner, peaks at 42 mm and completely oxidizes by 52 mm. However, increasing the proportion of IBE shows a decrease in not only the peak soot formation, but also the rate at which soot formation and oxidation occurs. The soot formation and oxidation rates are reflected in the ascending and descending slope of the curves respectively shown in ***Figure 26***. As a result of IBE addition, peak soot formation reaches 0.031 ppm at IBE0 and decreases nearly by 68% to 0.01 ppm at IBE100.

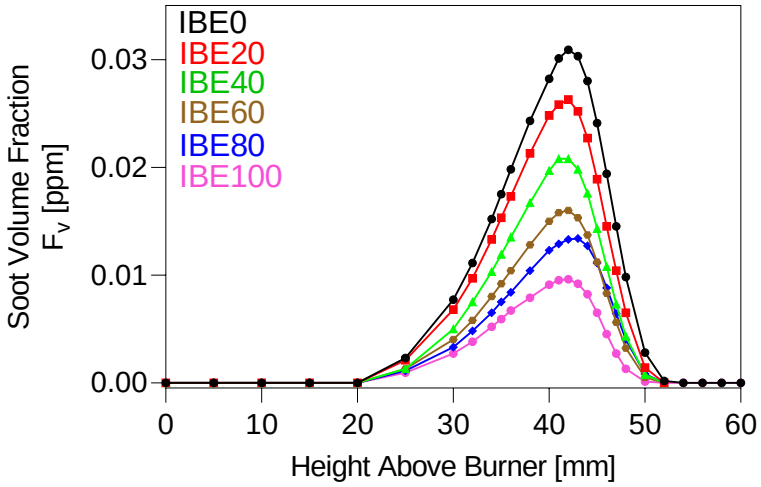

Figure 26: Radially integrated soot volume fraction distribution across as a function of height above burner for IBE/surrogate diesel blends

Figure 27 shows a comparison between experimentally measured and numerically simulated estimations of YSI for test mixtures ranging from IBE0 to IBE100. Error bars for measured data points have been calculated from standard deviation of YSIs from 60 images. For both the experiments and the numerical model, the upper and lower bounds of the YSI scale are kept consistent (i.e. YSI = 0 for hexane and YSI = 100 for benzene). Consequently, the experimental and numerical results show that the sooting propensity of the fuel mixtures tends to decrease in

YSI value as more IBE is added to the diesel surrogate mixture. Interestingly, the measured YSI of IBE100 (YSI_{IBE100} = -9.29) is similar to the predicted YSI value of -7 using the averaging method [24] (also shown in ***Figure 27***) incorporating YSI of individual components of the IBE mixture i.e. iso-propanol (YSI = -8.51), n-butanol (YSI = -6.38), and ethanol (YSI = -12.77). The larger YSI value of n-butanol compared to that of isopropanol suggests that carbon content of an alcohol molecule has a bigger role in determining its sooting tendency compared to the alcohol's position in the carbon chain. Like IBE, the measured YSI value of surrogate diesel (YSI = 241.85) was not very far from the predicted value of 283 obtained from YSI of its individual components i.e. n-decane (YSI = 8.51) and 1-methylnaphthalene (YSI = 751). This suggests that the weighted averaging method is capable of precisely predicting YSI of fuel mixtures based on YSI of individual components. The simulated absolute magnitude of YSI with the model is reasonably accurate for all IBE mixture ratios with the maximum deviation being 17 YSI units at IBE100. The higher deviation in YSI at extreme proportion of IBE in the mixture suggests that the model has greater predicative capabilities with surrogate diesel kinetics compared to IBE in the current context and experimental study.

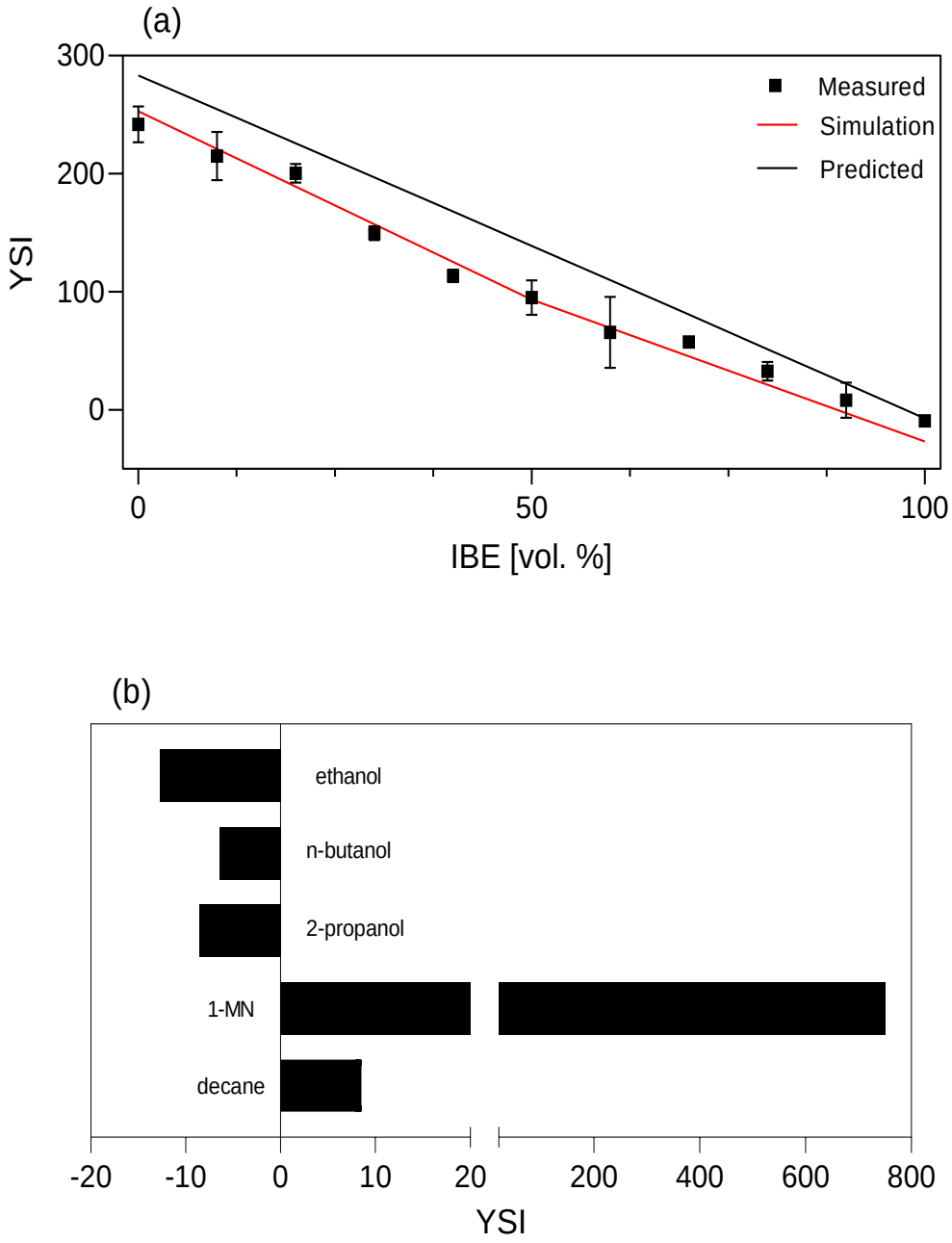

Figure 27: (a) Measured, simulated and predicted YSI of IBE/surrogate diesel blend (b) measured YSI of individual components

The accumulation and growth of heavy PAH species are traditionally responsible for soot formation, and their concentration is largely dependent on the initial fuel structure. Generally, the process of PAH formation begins with fuel decomposition by small radicals such as OH, O and H

forming a pool of small hydrocarbon radicals. These radicals then self-combine or react with other radicals to form the first aromatic ring which is benzene (C_6H_6). The growth process from benzene to heavy PAH species involves the combination of mostly C2 and C3 radicals with small PAH radicals, also known as the HACA mechanism. However, the choice of fuel employed plays a major role in determining the concentration of these small carbon radicals and thus the formation rate of benzene and PAH species. In order to investigate the chemical effect of IBE addition to surrogate diesel on total soot yield, it is therefore critical to study the formation route and distribution profile of benzene and PAH species along the flame. Hence, simulations were performed for an undoped methane flame as well as for flames doped with IBE0, IBE50 and IBE100 fuel mixture.

Methane, which is the base fuel, is an aliphatic compound and hence cannot form PAH species and soot without initially forming benzene. Therefore, benzene formation is the rate-limiting step for soot inception in an undoped methane flame and hence acted as a reference point to study soot formation in doped flames as well.

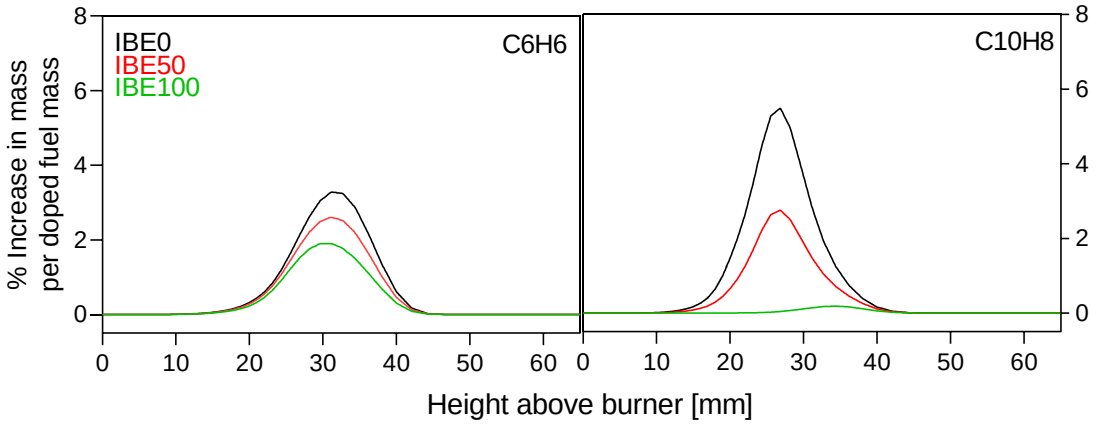

Figure 28: Computed percent increase in mass of benzene (left) and naphthalene (right) per doped fuel mass for IBE0, IBE50 and IBE100

Figure *28* shows that the addition of surrogate diesel (IBE0) in the methane flame enhances the concentration of benzene, thus complementing the trend observed in ***Figure 24*** where total soot yield is higher in IBE0 compared to the undoped flame. To gain an insight into the chemical effect of IBE0 addition, **Figure 29** shows the formation pathways of benzene from decomposition of methane as well as surrogate diesel components i.e. n-decane and 1-methylnaphthalene. As seen in **Figure 29**, benzene is formed via the following sequence:

$CH_4 \longrightarrow CH_3 \longrightarrow C_2H_6 \longrightarrow C_2H_4 \longrightarrow C_2H_3 \longrightarrow C_2H_2 \longrightarrow pC_3H_4 \longrightarrow C_3H_3 \longrightarrow C_6H_6$

Hence, benzene formation initiates from production of methyl radical. Since methane is the only source of methyl radical formation in an undoped flame, the addition of IBE0 provides an additional pathway for methyl radical formation. **Figure 29** shows that decomposition of n-decane leads to the formation of several smaller carbon species such as nC_3H_7, nC_5H_{11}, nC_7H_{15}, and $nC_{10}H_{21}$. Among these species, $nC_{10}H_{21}$ further decomposes to form nC_5H_{11} which eventually produces nC_3H_7. Methyl radical accounts for 32% consumption of nC_3H_7 whereas the remaining is consumed by the formation of ethylene. Ethylene acts as a precursor for acetylene which reacts with methyl radical to form pC_3H_4 radical (R7). PC_3H_4 radical can subsequently form C_3H_3 radical via reaction R8. Finally, the recombination reaction of C_3H_3 radical (R9) leads to the formation of benzene.

$$CH_3 + C_2H_2 = pC_3H_4 + H \quad \text{(R7)}$$

$$pC_3H_4 = C_3H_3 + H \quad \text{(R8)}$$

$$2C_3H_3 = C_6H_6 \quad \text{(R9)}$$

Unlike n-decane, the decomposition of 1-methylnaphthalene can enhance benzene concentration by providing a novel pathway to form C_6H_5 radical which is otherwise absent in the undoped methane flame. This is due to the cyclic nature of C_6H_5 radical as a consequence of which it can

be easily formed by aromatic compounds such as 1-methylnaphthalene as compared to methane. A major product from 1-methylnaphthalene decomposition is $C_{11}H_9$ radical which can form C_6H_5 radical via the following reaction sequence:

$$C_{11}H_9 \longrightarrow C_{10}H_8 \longrightarrow C_6H_5$$

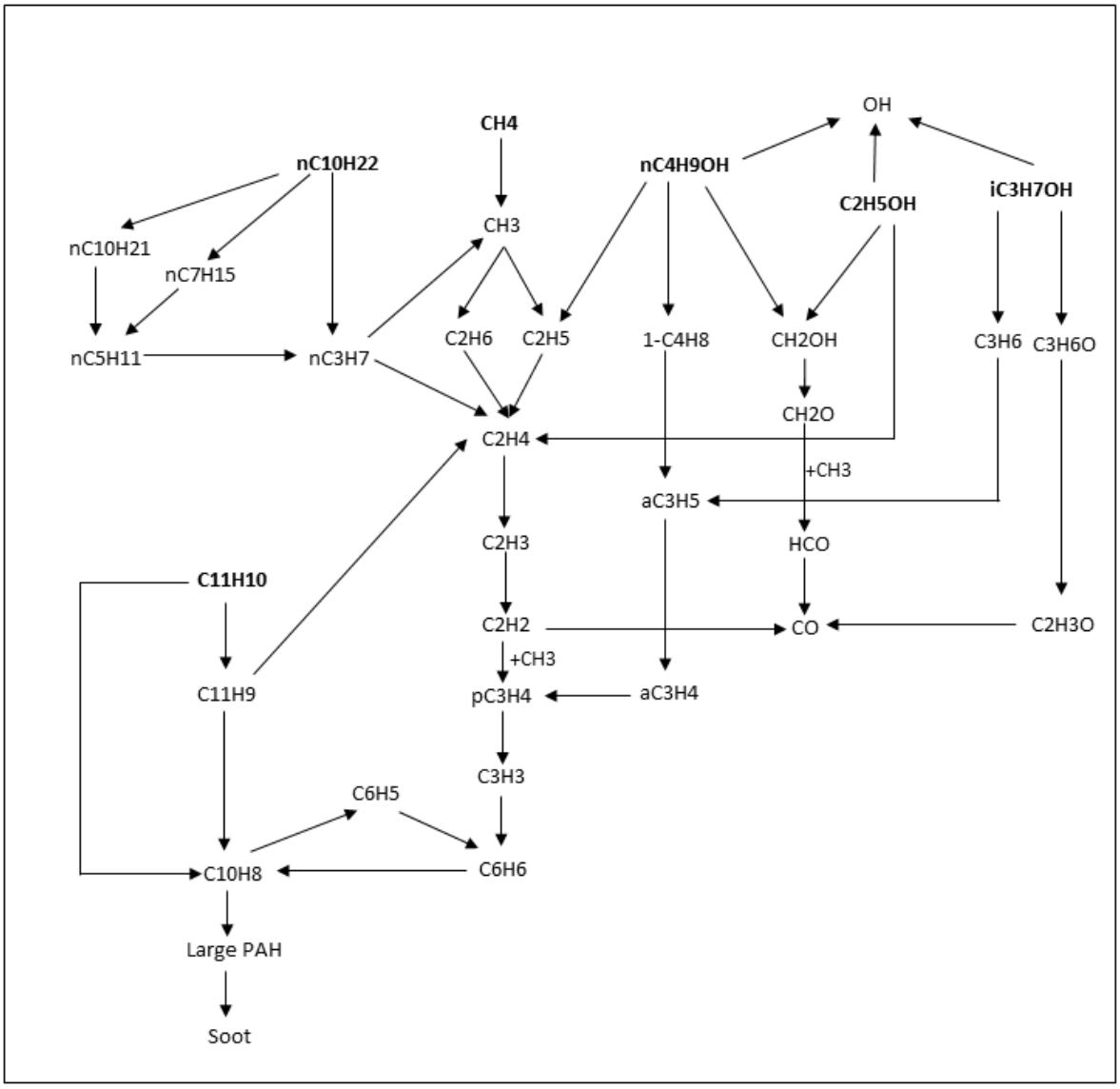

Figure 29: Fuel decomposition pathway of methane, surrogate diesel and IBE

C_6H_5 radical subsequently forms benzene via reaction R10. However, the major effect of 1-methylnaphthalene is observed in the PAH formation rather than that of benzene. Naphthalene ($C_{10}H_8$) being the simplest PAH specie has been chosen to illustrate this effect. As seen in **Figure 29**, naphthalene can be formed from 1-methylnaphthalene directly via reaction R11 or via an intermediate radical such as $C_{11}H_9$ (R12). The ability of 1-methylnapthalene to prematurely form naphthalene can be clearly seen in ***Figure 28*** where naphthalene peaks earlier than benzene in surrogate diesel doped flames such as IBE0 and IBE50.

$$H_2 + C_6H_5 = H + C_6H_6 \quad \text{(R10)}$$

$$H + C_{11}H_{10} = CH_3 + C_{10}H_8 \quad \text{(R11)}$$

$$C_{11}H_9 + CH_3 = C_{10}H_8 + C_2H_4 \quad \text{(R12)}$$

Figure 28 shows that the addition of IBE to surrogate diesel in the doped fuel mixture leads to a reduction in concentrations of both benzene and naphthalene. Also, concentrations of both benzene and naphthalene reduce uniformly as more IBE is added to the mixture, thus supporting the linear trend in soot reduction observed both experimentally and numerically in ***Figure 27***.

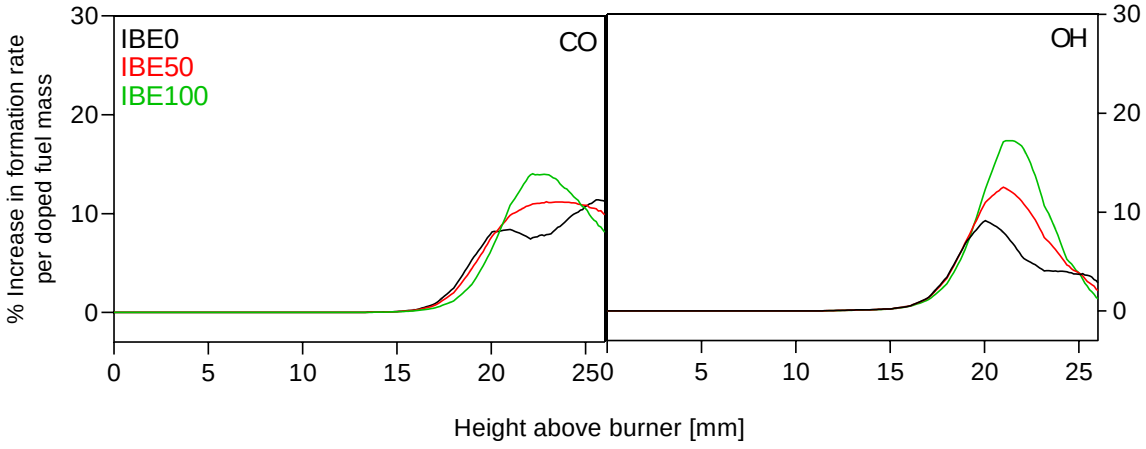

Figure 30: Computed percent increase in formation rate of CO and OH per doped fuel mass for IBE0, IBE50 and IBE100

The reduction in benzene and naphthalene concentration with IBE addition is primarily due to the reduced 1-methylnaphthalene content in the doped fuel mixture. As seen in **Figure 29**, unlike 1-methylnaphthalene, the decomposition pathways of IBE components do not have shorter formation route to naphthalene. Instead, it follows the traditional pathway to soot formation via HACA mechanism. This effect is apparent in **Figure *28*** where naphthalene starts forming after benzene in IBE100 flame in contrast to IBE0 flame. Similarly, IBE also cannot form C_6H_5 radical easily as compared to 1-methylnaphthalene mainly due to its non-aromatic nature. Hence, the major pathway of benzene formation in IBE100 flame is via C_3H_3 radical. As seen in **Figure 29**, all IBE components (i.e. isopropanol, butanol, and ethanol) produce C_3H_3 radical via different reaction pathways. In addition to C_3H_3 radical, they also form CO and OH radical due to the availability of oxygen atom in their fuel structure and is shown in **Figure *30*** where CO and OH formation rates are higher in flames doped with IBE. Since CO can only form CO_2 upon its further reaction, it retains the bonded carbon atom, thus depriving the latter's participation in soot formation. Due to the availability of fewer free carbon atoms, the production rate of C_3H_3 radical and benzene is lower in IBE100 flame as compared to IBE0 and IBE50. While greater CO production due to IBE suppresses soot formation, higher concentration of OH radicals increases soot oxidation by their interaction with mature soot particles. Hence, the addition of IBE to surrogate diesel in a methane flame leads to soot reduction via increasing the production rate of CO and OH while reducing that of benzene and PAH species.

4.2. Effect of carbon and oxygen loading on IBE's sooting tendency

IBE is made of three components i.e. isopropanol, butanol, and ethanol, which have different carbon and oxygen loading individually. Hence, changing the volumetric ratio of any one

of these components in the mixture affects the total carbon and oxygen loading of the mixture. However, which of these two parameters has higher impact on determining IBE's sooting tendency is unknown. Hence, two new IBE mixtures were prepared by modifying the volumetric ratio of butanol and ethanol in the current IBE mixture, while keeping isopropanol constant. While the first mixture had more ethanol and less butanol than that in the current IBE mixture, vice-versa was true for the second new mixture. For convenience of discussion, the original IBE mixture is referred to as ratio 1 whereas newly prepared IBE mixtures are referred to as ratio 2 and ratio 3. **Table *3*** presents the carbon and oxygen loading in a 300µL mixture of these three ratios.

Table 3: Carbon and oxygen loading of IBE ratios for 300µL mixture

Fuel	Carbon mass (g)	Oxygen mass (g)
Ratio 1	0.146	0.061
Ratio 2	0.130	0.075
Ratio 3	0.151	0.057

To determine the contribution of carbon loading of IBE, experiments were performed by doping the methane flame with each IBE ratio and measuring its sooting tendency. However, the liquid fuel was added such that the total carbon loading in the flame was the same for each IBE ratio.

Similar approach was adopted to determine the contribution of IBE's oxygen loading.

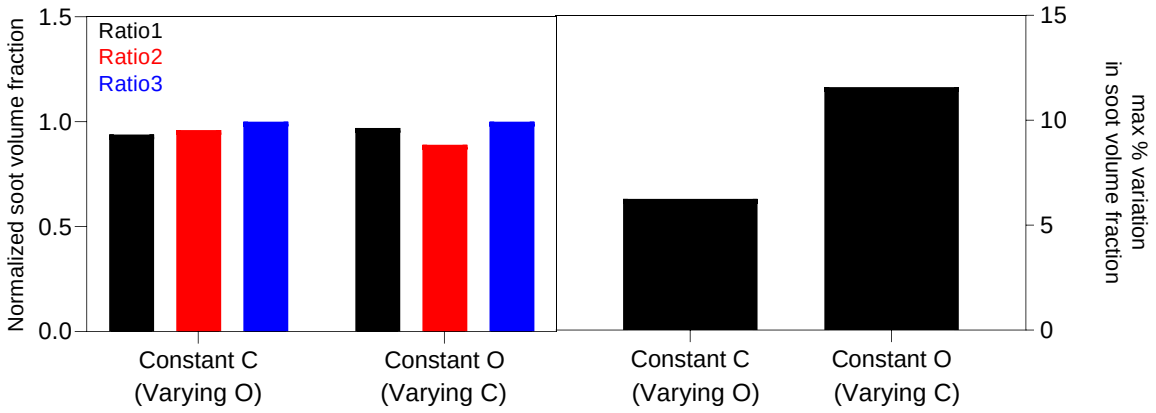

Figure 31: Normalized soot volume fraction for three IBE ratios (left) and maximum % variation in soot volume fraction (right) at constant C and O

The left graph of ***Figure 31*** shows soot volume fraction values (normalized to the largest value in respective experiment set) for three IBE ratios from the two sets of experiments (i.e. constant carbon and constant oxygen). The right graph of ***Figure 31*** shows the calculated difference between the highest and lowest value of soot volume fraction in each set. Since soot volume fraction increases by a maximum 6.5% when carbon loading of the flame is kept constant as opposed to 11.5% in constant oxygen loaded flame, it can be concluded that carbon has higher impact on determining total soot yield in the flame.

4.3. Effect of CO_2 addition to oxidizer stream

Figure 32 shows measured contour plots of soot volume fraction for IBE0 and IBE100 as a function of CO_2 dilution rate. It can be clearly seen that as CO_2 is added to the oxidizer stream of the co-flow burner, overall soot production within the flames decreases, regardless of IBE blend mixture ratio. Additionally, despite maintaining the overall oxidizer flow rate constant, the addition of the CO_2 mass in the oxidizer stream causes an increase in overall flame height. For

instance, at the maximum 9% dilution rate, it can be shown that the flame height for IBE0 increased to 58 mm compared to 52 mm without any dilution. According to a previous study, CO_2 dilution delays soot inception process through thermal and chemical effects and hence leads to longer flames [76]. In addition, the flame height for IBE0 is always visibly greater than that for IBE100. This could probably be due to their stark difference in soot load which contributes to lower flame temperature in IBE0, resulting in delayed soot oxidation and thus longer flame.

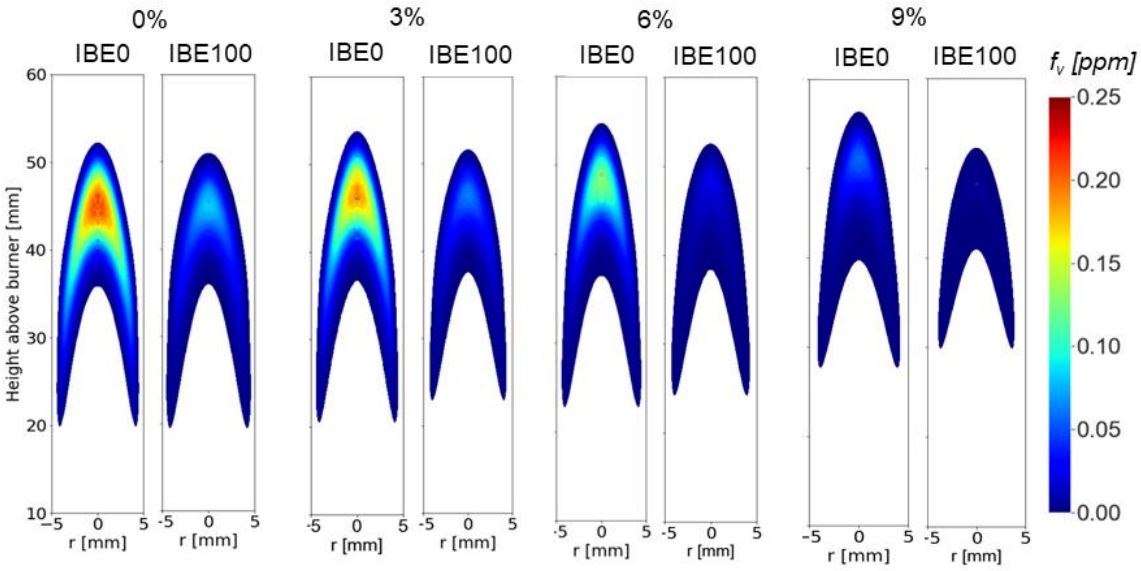

Figure 32: Soot volume fraction map for IBE0 and IBE100 at different CO2 levels

Figure 33 shows radially integrated soot volume fraction as a function of flame height for changes in CO_2 dilution rate for IBE0 and IBE100. It can be observed again that increasing the addition of CO_2 dilution causes a reduction in soot formation rate and hence in magnitude of peak soot volume fraction. By increasing the dilution rate of CO_2 to 9%, peak soot volume fraction decreased by nearly 87% for IBE0, and nearly 97% for IBE100. Also, due to the change in flame

height, peak soot formation is observed to proportionally shift towards higher locations in the flame. This also causes, soot oxidation region, which is where soot oxidation dominates soot formation, to shift downstream in the flame. In addition, soot oxidation rate is greatly reduced with CO_2 dilution, which is shown by the spread of lower soot concentration over an equal length of the flame. Despite the flame distance where soot survives being equal at different CO_2 dilution rates, the differing soot formation and oxidation rates show the effect of CO_2 on soot residence time in the flame. The addition of CO_2 leads to a longer residence time for soot owing to its thermal effect which lowers the axial flow velocity.

However, for a given CO_2 dilution rate, the rate of soot formation decreases as the proportion of IBE increases in the test mixture. Despite this, nearly 100% reduction in peak soot volume fraction was observed at a maximum dilution rate of 9% compared to 68% reduction at no dilution when the test mixture changed from IBE0 to IBE100.

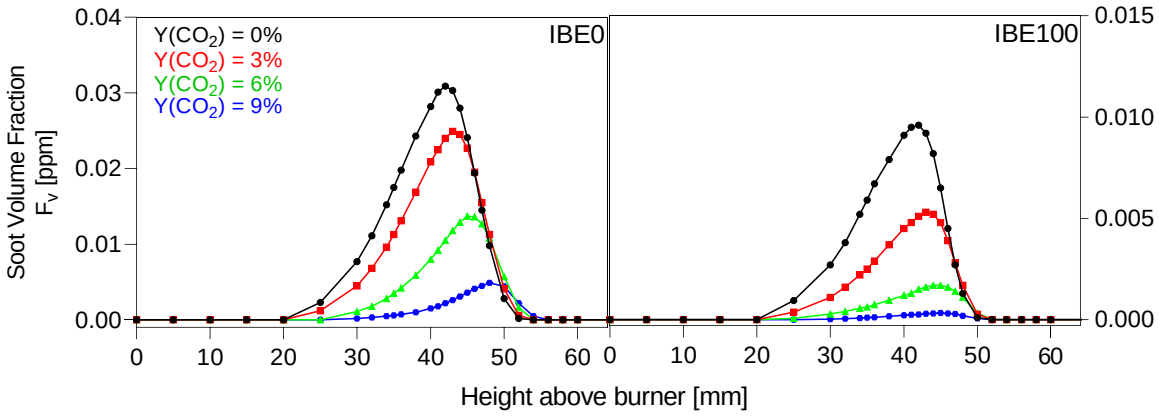

Figure 33: Radially integrated soot volume fraction distribution along different heights above the burner for different CO2 mass fractions in the air stream for IBE0 and IBE100

Figure 34 shows a comparison of experimentally and numerically derived YSI values for IBE/diesel surrogate blends as a function of CO_2 dilution rate. The model qualitatively predicts both the reduction in sooting propensity as CO_2 dilution rate increases for a given IBE blend ratio,

and the decrease in sooting propensity as IBE blend ratio increases for a given dilution rate. Both measured and simulated YSI curve show the decrease in the slope of the YSI curve and hence the rate of soot reduction as CO_2 dilution rate increases. This can be attributed to the dominant effect of CO_2 dilution over IBE addition on soot reduction. For instance, the slope of the YSI curve at Y_{CO2} = 9% is nearly flat due to the negligible amount of soot at IBE0, thus any further addition of IBE to mixture will result in very slight reduction in soot. While the simulation always predicts a linear trend in soot reduction with IBE addition at any CO_2 concentration, this is not true in the experiment where a non-linear trend is observed at Y_{CO2} = 9%. This could be due to the inability of the camera to detect the difference in soot loading in the flames doped with mixtures with high IBE concentration, thus also explaining a very high deviation in YSI between the measurement and simulation for such conditions.

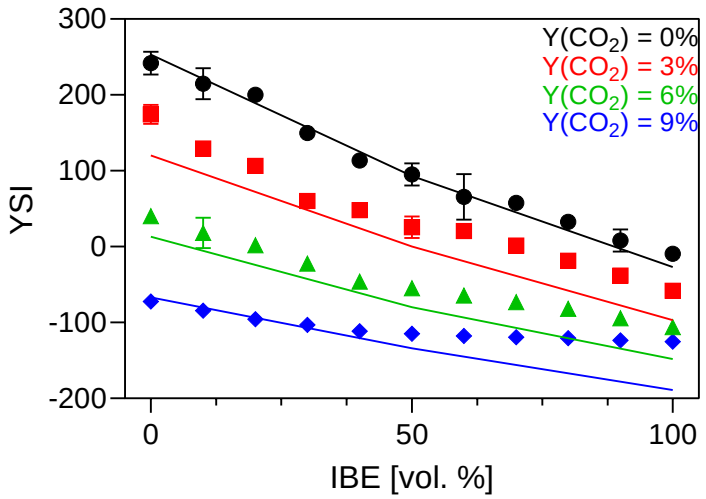

Figure 34: Measured (points) and simulated (solid lines) YSI values for IBE/surrogate diesel blends for different CO2 mass fractions in the air stream

To study the soot reduction effect of CO_2 addition in the oxidizer stream of the burner, simulations were performed for doped flames at CO_2 dilution rates replicating the experiments.

Since the CO_2 effects were found to remain constant regardless of the concentration of IBE in the doped fuel mixture, IBE50 has been chosen to illustrate these effects. As seen in ***Figure 35***, the concentrations of benzene and naphthalene decrease when more CO_2 is added in the oxidizer stream. Also, the delay in the processes of soot inception and oxidation observed in the experiment are reflected by the shift in the initial formation and peak locations of both of these species downstream in the CO_2 diluted flames.

Figure 36 shows the computed temperature profiles for the four simulated flames. Owing to its high specific heat capacity, CO_2 addition causes temperature to drop across the entire flame. The lower flame temperature slows down the fuel decomposition process, thus causing a delay in soot inception. The thermal effect of CO_2 is deemed to be the dominant factor for soot reduction as it lowers the reaction rates of the fuel decomposition products which later form benzene and naphthalene. However, ROP analysis indicates that the chemical effect of CO_2 also plays a role in soot reduction via reactions R14 and R15.

$$CO_2 + H = CO + OH \quad \text{(R14)}$$

$$CO_2 + CH_2{*} = CH_2O + CO \quad \text{(R15)}$$

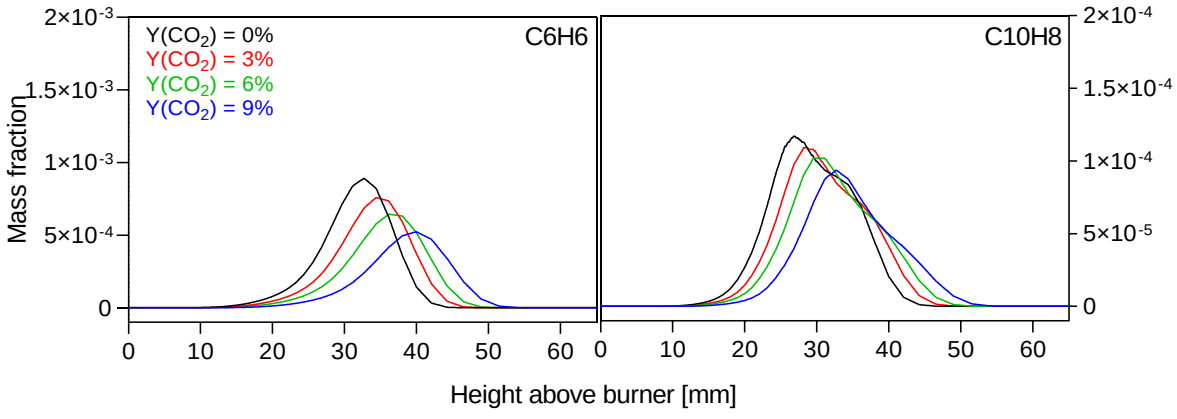

Figure 35: Computed mass fraction profiles of benzene and naphthalene along the flame centerline for IBE50 at different CO2 mass fractions

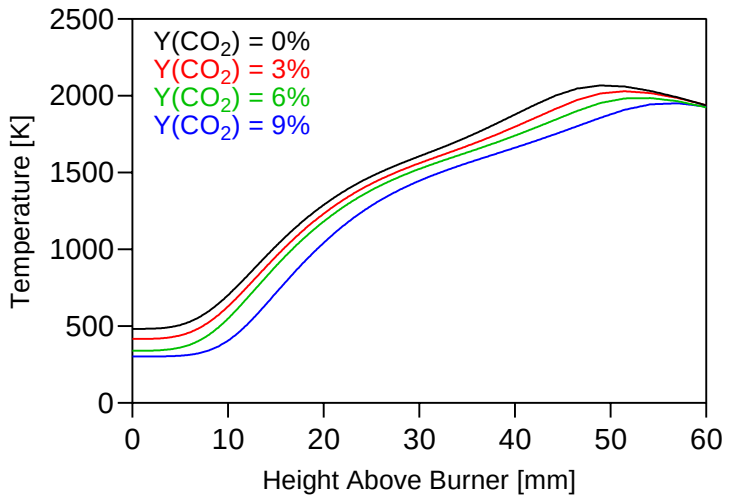

Figure 36: Computed temperature profile along the flame centerline for IBE50 at different CO2 mass fractions

In reaction R14, the production of OH radicals can lead to soot reduction via oxidative attack of PAH species and mature soot particles. This reaction occurs only beyond 33mm above the burner exit at all four conditions and is evident in ***Figure 35*** where the reduction in magnitude of secondary peak of naphthalene is much more significant than that in the initial peak which occurs before 33mm.

Similarly, in reaction R15, the consumption of activated methylene (CH_2*) by CO_2 can prevent the former to react with acetylene to form propargyl radical (R16).

$CH_2^* + C_2H_2 = C_3H_3$ (R16)

Propargyl radical is not only responsible for benzene formation but also for soot surface growth by its combination with PAH species and soot particles. Hence, its lower formation rate via R16 leads to reduction in benzene concentration as well as soot surface growth rate. These two effects combinedly lower the total soot yield in the flame.

CHAPTER 5: CONCLUSION

5.1. Summary

Experimental and numerical studies were carried out in a laminar co-flow diffusion methane flame to study the soot reduction effect of IBE addition to surrogate diesel as well as the individual effect of carbon and oxygen loading of IBE on its sooting tendency. The setup also allowed to add CO_2 to the oxidizer stream of the burner and thus study its effect on soot inhibition. While sooting tendencies were measured in terms of YSI by utilizing color ratio pyrometry technique with a consumer grade digital camera, simulations were performed with laminarSMOKE++ to investigate the chemical effect of fuel blending and CO_2 addition. At the end of the research work described in this thesis, the following conclusions were drawn:

1) IBE addition to surrogate diesel in the doped fuel mixture enhances soot reduction and the increase in soot reduction is linear with the volumetric ratio of IBE in the fuel blend.
2) Simulations indicate that the addition of IBE reduces benzene and PAH formation primarily by reducing the 1-methylnaphthalene content in the doped fuel mixture, thus reducing the effectiveness of direct formation pathways of C_6H_5 radical and naphthalene. However, the enhanced production of CO and OH radical from IBE also plays a role in soot reduction by preventing carbon atom attached to oxygen from participating in benzene formation and attacking mature soot particles respectively.
3) Carbon loading of IBE has higher impact on determining total soot yield in the flame as compared to oxygen.
4) CO_2 addition to the oxidizer stream results in soot reduction as well as delay in soot nucleation and oxidation. The thermal effect of CO_2 is primarily responsible for reduced

rate of reactions leading to soot. However, CO_2 also contributes to soot reduction chemically by producing OH radicals and consuming activated methylene. While the production of OH radicals leads to oxidative attack of PAH species and soot particles, the consumption of activated methylene lowers the production rate of propargyl radical, thus lowering benzene formation and soot surface growth rates.

5.2. Recommendations for future work

While IBE is certainly an attractive biofuel due to its soot reducing potential, several other oxygenated biofuels are currently being produced whose sooting tendencies when blended with diesel are yet to be quantified. To the best of the author's knowledge, some of these biofuels are butyl acetate, n-butyl butyrate, n-butyl lactate, and 2,3-butanediol. Hence, future soot studies of these biofuels by implementing the current experimental methodology will not only contribute to the existent YSI database but will also determine if any synergistic effect exists between the biofuel and diesel when mixed. Most importantly, the measured dataset will enable numerical studies to benchmark current as well as future kinetic mechanisms for reliable interpretation of reaction kinetics of these biofuels when mixed with diesel.

In addition to oxygenated fuels, several technologies have emerged in the past as a part of strategic efforts to limit soot emissions. One of them is plasma assisted combustion. Hence, a potential avenue of future research work is the investigation of the effect of plasma on soot formation in diffusion flames. Previous experimental plasma study on diffusion flame has been performed by adopting dielectric barrier discharge technique [77]. While it showed nonthermal plasma to have PAH and soot suppression effects on a hydrocarbon fuel, its effect on oxygenated

fuels is yet to be seen. Performing such studies in the current experimental setup however requires modification of the burner to install a source for plasma generation.

REFERENCES

[1] E. Sasser *et al.*, "Report to Congress on Black Carbon," 2012.

[2] J. Weidman and S. Marshall, "Soot Pollution 101," *Center for American Progress*, Aug. 10, 2012.

[3] X. Wu, R. C. Nethery, M. B. Sabath, D. Braun, and F. Dominici, "Air pollution and COVID-19 mortality in the United States: Strengths and limitations of an ecological regression analysis," *Science Advances*, vol. 6, no. 45, Nov. 2020, doi: 10.1126/sciadv.abd4049.

[4] T. C. Bond *et al.*, "Bounding the role of black carbon in the climate system: A scientific assessment," *Journal of Geophysical Research: Atmospheres*, vol. 118, no. 11, Jun. 2013, doi: 10.1002/jgrd.50171.

[5] B. Karcher, O. Mohler, P. J. DeMott, S. Pechtl, and F. Yu, "Insights into the role of soot aerosols in cirrus cloud formation," *Atmospheric Chemistry and Physics Discussions 7.3*, pp. 7843–7905, 2007.

[6] "Co-Optimization of Fuels & Engines." Office of Energy Efficiency & Renewable Energy, 2016.

[7] D. J. Gaspar *et al.*, "Top Ten Blendstocks Derived From Biomass For Turbocharged Spark Ignition Engines: Bio-blendstocks With Potential for Highest Engine Efficiency," Richland, WA (United States), Sep. 2019. doi: 10.2172/1567705.

[8] I. Veza, M. F. Muhamad Said, and Z. A. Latiff, "Recent advances in butanol production by acetone-butanol-ethanol (ABE) fermentation," *Biomass and Bioenergy*, vol. 144, p. 105919, Jan. 2021, doi: 10.1016/J.BIOMBIOE.2020.105919.

[9] H. Wu, T. H. Lee, C. Lee, F. Liu, and B. Sun, "Optical soot measurement of bio-butanol upstream product, ABE (Acetone–Butanol–Ethanol), under diesel-like conditions," *Fuel*, vol. 181, Oct. 2016, doi: 10.1016/j.fuel.2016.04.092.

[10] P. Wang, J. Feng, L. Guo, O. Fasina, and Y. Wang, "Engineering Clostridium saccharoperbutylacetonicum for High Level Isopropanol-Butanol-Ethanol (IBE) Production from Acetic Acid Pretreated Switchgrass Using the CRISPR-Cas9 System," *ACS Sustainable Chemistry & Engineering*, vol. 7, no. 21, Nov. 2019, doi: 10.1021/acssuschemeng.9b05336.

[11] G. Knothe, "Georges Chavanne and the first biodiesel," *INFORM International News on Fats, Oils, and Related Materials*, vol. 28, no. 7, pp. 21–24, Jul. 2017, doi: 10.21748/inform.07.2017.21.

[12] H. A. Alalwan, A. H. Alminshid, and H. A. S. Aljaafari, "Promising evolution of biofuel generations. Subject review," *Renewable Energy Focus*, vol. 28, pp. 127–139, Mar. 2019, doi: 10.1016/J.REF.2018.12.006.

[13] M. S. Pishvaee, S. Mohseni, and S. Bairamzadeh, "Uncertainties in biofuel supply chain," *Biomass to Biofuel Supply Chain Design and Planning Under Uncertainty*, pp. 65–93, Jan. 2021, doi: 10.1016/B978-0-12-820640-9.00004-0.

[14] A. Sun, R. Davis, M. Starbuck, A. Ben-Amotz, R. Pate, and P. T. Pienkos, "Comparative cost analysis of algal oil production for biofuels," *Energy*, vol. 36, no. 8, pp. 5169–5179, Aug. 2011, doi: 10.1016/J.ENERGY.2011.06.020.

[15] P. Tandon and Q. Jin, "Microalgae culture enhancement through key microbial approaches," *Renewable and Sustainable Energy Reviews*, vol. 80, pp. 1089–1099, Dec. 2017, doi: 10.1016/J.RSER.2017.05.260.

[16] C. H. Hsieh and W. T. Wu, “Cultivation of microalgae for oil production with a cultivation strategy of urea limitation,” *Bioresource Technology*, vol. 100, no. 17, pp. 3921–3926, Sep. 2009, doi: 10.1016/J.BIORTECH.2009.03.019.
[17] B. Abdullah *et al.*, “Fourth generation biofuel: A review on risks and mitigation strategies,” *Renewable and Sustainable Energy Reviews*, vol. 107, pp. 37–50, Jun. 2019, doi: 10.1016/J.RSER.2019.02.018.
[18] H. F. Calcote and D. M. Manos, “Effect of molecular structure on incipient soot formation,” *Combustion and Flame*, vol. 49, no. 1–3, pp. 289–304, Jan. 1983, doi: 10.1016/0010-2180(83)90172-4.
[19] E. J. Barrientos, M. Lapuerta, and A. L. Boehman, “Group additivity in soot formation for the example of C-5 oxygenated hydrocarbon fuels,” *Combustion and Flame*, vol. 160, no. 8, pp. 1484–1498, Aug. 2013, doi: 10.1016/J.COMBUSTFLAME.2013.02.024.
[20] R. Lemaire, D. Lapalme, and P. Seers, “Analysis of the sooting propensity of C-4 and C-5 oxygenates: Comparison of sooting indexes issued from laser-based experiments and group additivity approaches,” *Combustion and Flame*, vol. 162, no. 9, pp. 3140–3155, Sep. 2015, doi: 10.1016/J.COMBUSTFLAME.2015.03.018.
[21] S. P. Crossley, W. E. Alvarez, and D. E. Resasco, “Novel Micropyrolyis Index (MPI) to Estimate the Sooting Tendency of Fuels,” *Energy & Fuels*, vol. 22, no. 4, pp. 2455–2464, May 2008, doi: 10.1021/ef800058y.
[22] C. MCENALLY and L. PFEFFERLE, “Improved sooting tendency measurements for aromatic hydrocarbons and their implications for naphthalene formation pathways,” *Combustion and Flame*, vol. 148, no. 4, Mar. 2007, doi: 10.1016/j.combustflame.2006.11.003.
[23] D. D. Das *et al.*, “Sooting tendencies of diesel fuels, jet fuels, and their surrogates in diffusion flames,” *Fuel*, vol. 197, pp. 445–458, Jun. 2017, doi: 10.1016/J.FUEL.2017.01.099.
[24] C. S. McEnally and L. D. Pfefferle, “Sooting Tendencies of Oxygenated Hydrocarbons in Laboratory-Scale Flames,” *Environmental Science & Technology*, vol. 45, no. 6, pp. 2498–2503, Feb. 2011, doi: 10.1021/es103733q.
[25] K. M. Allan, J. R. Kaminski, J. C. Bertrand, J. Head, and P. B. Sunderland, “Laminar Smoke Points of Wax Candles,” *Combustion Science and Technology*, vol. 181, no. 5, pp. 800–811, Apr. 2009, doi: 10.1080/00102200902935512.
[26] R. Lemaire, E. Therssen, and P. Desgroux, “Effect of ethanol addition in gasoline and gasoline–surrogate on soot formation in turbulent spray flames,” *Fuel*, vol. 89, no. 12, pp. 3952–3959, Dec. 2010, doi: 10.1016/J.FUEL.2010.06.031.
[27] Z. Gao, L. Zhu, X. Zou, C. Liu, B. Tian, and Z. Huang, “Soot reduction effects of dibutyl ether (DBE) addition to a biodiesel surrogate in laminar coflow diffusion flames,” *Proceedings of the Combustion Institute*, vol. 37, no. 1, pp. 1265–1272, Jan. 2019, doi: 10.1016/J.PROCI.2018.05.083.
[28] B. Chen, X. Liu, H. Liu, H. Wang, D. C. Kyritsis, and M. Yao, “Soot reduction effects of the addition of four butanol isomers on partially premixed flames of diesel surrogates,” *Combustion and Flame*, vol. 177, pp. 123–136, Mar. 2017, doi: 10.1016/J.COMBUSTFLAME.2016.12.012.
[29] M. K. Tran, D. Dunn-Rankin, and T. K. Pham, “Characterizing sooting propensity in biofuel–diesel flames,” *Combustion and Flame*, vol. 159, no. 6, pp. 2181–2191, Jun. 2012, doi: 10.1016/J.COMBUSTFLAME.2012.01.008.

[30] A. Cuoci *et al.*, “Experimental and detailed kinetic modeling study of PAH formation in laminar co-flow methane diffusion flames,” *Proceedings of the Combustion Institute*, vol. 34, no. 1, pp. 1811–1818, Jan. 2013, doi: 10.1016/J.PROCI.2012.05.085.
[31] X. Cheng, Z. Gao, F. Ren, S. Rigopoulos, L. Zhu, and Z. Huang, “Experimental and kinetic modeling study on sooting tendencies of alkylbenzene isomers,” *Fuel*, vol. 283, p. 118873, Jan. 2021, doi: 10.1016/J.FUEL.2020.118873.
[32] H. Wang and M. Frenklach, “A detailed kinetic modeling study of aromatics formation in laminar premixed acetylene and ethylene flames,” *Combustion and Flame*, vol. 110, no. 1–2, pp. 173–221, Jul. 1997, doi: 10.1016/S0010-2180(97)00068-0.
[33] F. Liu, Y. Hua, H. Wu, C. fon Lee, and Z. Shi, “Experimental and kinetic studies of soot formation in methanol-gasoline coflow diffusion flames,” *Journal of the Energy Institute*, vol. 92, no. 1, pp. 38–50, Feb. 2019, doi: 10.1016/J.JOEI.2017.12.002.
[34] C. Zhang, A. Atreya, and K. Lee, “Sooting structure of methane counterflow diffusion flames with preheated reactants and dilution by products of combustion,” *Symposium (International) on Combustion*, vol. 24, no. 1, pp. 1049–1057, Jan. 1992, doi: 10.1016/S0082-0784(06)80124-4.
[35] D. X. Du, R. L. Axelbaum, and C. K. Law, “The influence of carbon dioxide and oxygen as additives on soot formation in diffusion flames,” *Symposium (International) on Combustion*, vol. 23, no. 1, pp. 1501–1507, Jan. 1991, doi: 10.1016/S0082-0784(06)80419-4.
[36] Q. Tang, J. Mei, and X. You, “Effects of CO2 addition on the evolution of particle size distribution functions in premixed ethylene flame,” *Combustion and Flame*, vol. 165, pp. 424–432, Mar. 2016, doi: 10.1016/J.COMBUSTFLAME.2015.12.026.
[37] P. Liu *et al.*, “Chemical Mechanism of Exhaust Gas Recirculation on Polycyclic Aromatic Hydrocarbons Formation Based on Laser-Induced Fluorescence Measurement,” *Energy & Fuels*, vol. 32, no. 6, pp. 7112–7124, May 2018, doi: 10.1021/acs.energyfuels.8b00422.
[38] K. P. SCHUG, Y. MANHEIMER-TIMNAT, P. YACCARINO, and I. GLASSMAN, “Sooting Behavior of Gaseous Hydrocarbon Diffusion Flames and the Influence of Additives,” *Combustion Science and Technology*, vol. 22, no. 5–6, pp. 235–250, Jun. 1980, doi: 10.1080/00102208008952387.
[39] F. Liu, H. Guo, G. J. Smallwood, and Ö. L. Gülder, “The chemical effects of carbon dioxide as an additive in an ethylene diffusion flame: implications for soot and NOx formation,” *Combustion and Flame*, vol. 125, no. 1–2, pp. 778–787, Apr. 2001, doi: 10.1016/S0010-2180(00)00241-8.
[40] C. A. Hoerlle and F. M. Pereira, “Effects of CO2 addition on soot formation of ethylene non-premixed flames under oxygen enriched atmospheres,” *Combustion and Flame*, vol. 203, pp. 407–423, May 2019, doi: 10.1016/J.COMBUSTFLAME.2019.02.016.
[41] N. M. Mahmoud, F. Yan, M. Zhou, L. Xu, and Y. Wang, “Coupled Effects of Carbon Dioxide and Water Vapor Addition on Soot Formation in Ethylene Diffusion Flames,” *Energy & Fuels*, vol. 33, no. 6, pp. 5582–5596, May 2019, doi: 10.1021/acs.energyfuels.9b00192.
[42] Y. Li *et al.*, “Combustion, performance and emissions characteristics of a spark-ignition engine fueled with isopropanol-n-butanol-ethanol and gasoline blends,” *Fuel*, vol. 184, pp. 864–872, Nov. 2016, doi: 10.1016/J.FUEL.2016.07.063.

[43] T. H. Lee, H. Wu, A. Hansen, T. Lee, and G. Li, “Comparison Study on Combustion and Emission Characteristics of ABE/IBE-Diesel Blends in a Common-Rreail Diesel Engine,” Oct. 2017. doi: 10.4271/2017-01-2321.
[44] G. Li, Z. Liu, T. H. Lee, C. F. Lee, and C. Zhang, “Effects of dilute gas on combustion and emission characteristics of a common-rail diesel engine fueled with isopropanol-butanol-ethanol and diesel blends,” *Energy Conversion and Management*, vol. 165, pp. 373–381, Jun. 2018, doi: 10.1016/J.ENCONMAN.2018.03.073.
[45] G. Li, T. H. Lee, Z. Liu, C. F. Lee, and C. Zhang, “Effects of injection strategies on combustion and emission characteristics of a common-rail diesel engine fueled with isopropanol-butanol-ethanol and diesel blends,” *Renewable Energy*, vol. 130, pp. 677–686, Jan. 2019, doi: 10.1016/J.RENENE.2018.06.099.
[46] T. H. Lee, G. Li, J. Yan, and C. Zhang, “Spray, Combustion, and Flame Structures of High-Ratio Isopropanol-Butanol-Ethanol (IBE)/Diesel Blends in a Constant Volume Chamber,” *Energy & Fuels*, vol. 34, no. 7, Jul. 2020, doi: 10.1021/acs.energyfuels.0c01304.
[47] T. H. Lee, A. C. Hansen, G. Li, and T. Lee, “Effects of isopropanol-butanol-ethanol and diesel fuel blends on combustion characteristics in a constant volume chamber,” *Fuel*, vol. 254, p. 115613, Oct. 2019, doi: 10.1016/J.FUEL.2019.06.021.
[48] G. Li, T. H. Lee, and C. Zhang, “Optical investigation on impacts of component ratio on spray, combustion and flame structure of isopropanol-butanol-ethanol (IBE)/diesel blends,” *Fuel*, vol. 280, p. 118602, Nov. 2020, doi: 10.1016/J.FUEL.2020.118602.
[49] J. Hu, S. Abubakar, and Y. Li, “A novel reduced i-propanol-n-butanol-ethanol (IBE)/diesel mechanism for engine combustion and emissions prediction,” *Fuel*, vol. 278, p. 118291, Oct. 2020, doi: 10.1016/J.FUEL.2020.118291.
[50] E. RANZI, A. FRASSOLDATI, A. STAGNI, M. PELUCCHI, A. CUOCI, and T. FARAVELLI, “Reduced Kinetic Schemes of Complex Reaction Systems: Fossil and Biomass-Derived Transportation Fuels,” *International Journal of Chemical Kinetics*, vol. 46, no. 9, Sep. 2014, doi: 10.1002/kin.20867.
[51] A. Stagni, A. Cuoci, A. Frassoldati, T. Faravelli, and E. Ranzi, “Lumping and Reduction of Detailed Kinetic Schemes: an Effective Coupling,” *Industrial & Engineering Chemistry Research*, vol. 53, no. 22, Jun. 2014, doi: 10.1021/ie403272f.
[52] P. Dagaut, M. Reuillon, and M. Cathonnet, “Experimental study of the oxidation of n-heptane in a jet stirred reactor from low to high temperature and pressures up to 40 atm,” *Combustion and Flame*, vol. 101, no. 1–2, pp. 132–140, Apr. 1995, doi: 10.1016/0010-2180(94)00184-T.
[53] H. P. Ramirez L., K. Hadj-Ali, P. Diévart, G. Moréac, and P. Dagaut, “Kinetics of Oxidation of Commercial and Surrogate Diesel Fuels in a Jet-Stirred Reactor: Experimental and Modeling Studies,” *Energy & Fuels*, vol. 24, no. 3, Mar. 2010, doi: 10.1021/ef9015526.
[54] C. Saggese *et al.*, “Kinetic modeling of particle size distribution of soot in a premixed burner-stabilized stagnation ethylene flame,” *Combustion and Flame*, vol. 162, no. 9, pp. 3356–3369, Sep. 2015, doi: 10.1016/J.COMBUSTFLAME.2015.06.002.
[55] W. Pejpichestakul *et al.*, “Examination of a soot model in premixed laminar flames at fuel-rich conditions,” *Proceedings of the Combustion Institute*, vol. 37, no. 1, 2019, doi: 10.1016/j.proci.2018.06.104.

[56] G. Wang, “Demosaicking with two-dimensional continuous 3 × 3 order hidden Markov model,” *EURASIP Journal on Image and Video Processing*, vol. 2018, no. 1, p. 131, Dec. 2018, doi: 10.1186/s13640-018-0369-4.
[57] B. Ma, “Development of quantitative optical techniques for microgravity combustion and sooty flame characterization,” Yale University, 2013.
[58] B. Ma and M. B. Long, “Absolute light calibration using S-type thermocouples,” *Proceedings of the Combustion Institute*, vol. 34, no. 2, Jan. 2013, doi: 10.1016/j.proci.2012.05.030.
[59] S. S. Krishnan, K.-C. Lin, and G. M. Faeth, “Optical Properties in the Visible of Overfire Soot in Large Buoyant Turbulent Diffusion Flames,” *Journal of Heat Transfer*, vol. 122, no. 3, Aug. 2000, doi: 10.1115/1.1288025.
[60] “Determination of the wavelength dependence of refractive indices of flame soot,” *Proceedings of the Royal Society of London. Series A: Mathematical and Physical Sciences*, vol. 430, no. 1880, pp. 577–591, Sep. 1990, doi: 10.1098/rspa.1990.0107.
[61] D. D. Hickstein, S. T. Gibson, R. Yurchak, D. D. Das, and M. Ryazanov, “A direct comparison of high-speed methods for the numerical Abel transform,” *Review of Scientific Instruments*, vol. 90, no. 6, p. 065115, Jun. 2019, doi: 10.1063/1.5092635.
[62] V. Dribinski, A. Ossadtchi, V. A. Mandelshtam, and H. Reisler, “Reconstruction of Abel-transformable images: The Gaussian basis-set expansion Abel transform method,” *Review of Scientific Instruments*, vol. 73, no. 7, pp. 2634–2642, Jul. 2002, doi: 10.1063/1.1482156.
[63] K. T. Walsh, J. Fielding, and M. B. Long, “Effect of light-collection geometry on reconstruction errors in Abel inversions,” *Optics Letters*, vol. 25, no. 7, p. 457, Apr. 2000, doi: 10.1364/OL.25.000457.
[64] D. D. Das, W. J. Cannella, C. S. McEnally, C. J. Mueller, and L. D. Pfefferle, “Two-dimensional soot volume fraction measurements in flames doped with large hydrocarbons,” *Proceedings of the Combustion Institute*, vol. 36, no. 1, pp. 871–879, Jan. 2017, doi: 10.1016/J.PROCI.2016.06.047.
[65] B. Tian, Y. Gao, C. Zhang, and S. Hochgreb, “Soot measurement in diluted methane diffusion flames by multi-pass extinction and laser-induced incandescence,” *Combustion and Flame*, vol. 192, pp. 224–237, Jun. 2018, doi: 10.1016/J.COMBUSTFLAME.2018.01.037.
[66] H. W. Coleman and W. G. Steele, *Experimental Validation, and Uncertainty Analysis for Engineers*, 3rd ed. John Wiley & Sons, 2009.
[67] A. Cuoci, A. Frassoldati, T. Faravelli, and E. Ranzi, “Numerical Modeling of Laminar Flames with Detailed Kinetics Based on the Operator-Splitting Method,” *Energy & Fuels*, vol. 27, no. 12, Dec. 2013, doi: 10.1021/ef4016334.
[68] A. Cuoci, A. Frassoldati, T. Faravelli, and E. Ranzi, “OpenSMOKE++: An object-oriented framework for the numerical modeling of reactive systems with detailed kinetic mechanisms,” *Computer Physics Communications*, vol. 192, Jul. 2015, doi: 10.1016/j.cpc.2015.02.014.
[69] A. Cuoci, A. Frassoldati, T. Faravelli, and E. Ranzi, “A computational tool for the detailed kinetic modeling of laminar flames: Application to C2H4/CH4 coflow flames,” *Combustion and Flame*, vol. 160, no. 5, May 2013, doi: 10.1016/j.combustflame.2013.01.011.
[70] “OpenFOAM, www.openfoam.org, 2011.”

[71] G. Strang, “On the Construction and Comparison of Difference Schemes,” *SIAM Journal on Numerical Analysis*, vol. 5, no. 3, pp. 506–517, Sep. 1968, doi: 10.1137/0705041.
[72] E. Ranzi, C. Cavallotti, A. Cuoci, A. Frassoldati, M. Pelucchi, and T. Faravelli, “New reaction classes in the kinetic modeling of low temperature oxidation of n-alkanes,” *Combustion and Flame*, vol. 162, no. 5, May 2015, doi: 10.1016/j.combustflame.2014.11.030.
[73] A. Nobili *et al.*, “On the radical behavior of large polycyclic aromatic hydrocarbons in soot formation and oxidation,” *Combustion and Flame*, vol. 235, p. 111692, Jan. 2022, doi: 10.1016/J.COMBUSTFLAME.2021.111692.
[74] C. R. Shaddix, “Correcting thermocouple measurements for radiation loss: a critical review,” 1999.
[75] M. Kashif, P. Guibert, J. Ô. Bonnety, and G. Legros, “Sooting tendencies of primary reference fuels in atmospheric laminar diffusion flames burning into vitiated air,” *Combustion and Flame*, vol. 161, no. 6, pp. 1575–1586, Jun. 2014, doi: 10.1016/J.COMBUSTFLAME.2013.12.009.
[76] M. S. Cha, S. M. Lee, K. T. Kim, and S. H. Chung, “Soot suppression by nonthermal plasma in coflow jet diffusion flames using a dielectric barrier discharge,” *Combustion and Flame*, vol. 141, no. 4, pp. 438–447, Jun. 2005, doi: 10.1016/J.COMBUSTFLAME.2005.02.002.
[77] R. Sumner, “Processing RAW Images in MATLAB,” 2014.

APPENDIX A: MATLAB CODE FOR IMAGE PROCESSING

The following MATLAB code has been referenced from [78] and was used to perform demosaicing of the raw flame image and split it into RGB images.

```
filename = 'filename.dng'; % Put file name here
warning off MATLAB:tifflib:TIFFReadDirectory:libraryWarning
t = Tiff(filename,'r');
offsets = getTag(t,'SubIFD');
setSubDirectory(t,offsets(1));
raw = read(t); % Create variable 'raw', the Bayer CFA data
close(t);
meta_info = imfinfo(filename);
% Crop to only valid pixels
x_origin = meta_info.SubIFDs{1}.ActiveArea(2)+1; % +1 due to MATLAB indexing
width = meta_info.SubIFDs{1}.DefaultCropSize(1);
y_origin = meta_info.SubIFDs{1}.ActiveArea(1)+1;
height = meta_info.SubIFDs{1}.DefaultCropSize(2);
raw = double(raw(y_origin:y_origin+height-1,x_origin:x_origin+width-1));
if isfield(meta_info.SubIFDs{1},'LinearizationTable')
ltab=meta_info.SubIFDs{1}.LinearizationTable;
raw = ltab(raw+1);
end
black = meta_info.SubIFDs{1}.BlackLevel(1);
saturation = meta_info.SubIFDs{1}.WhiteLevel;
lin_bayer = (raw-black)/(saturation-black);
lin_bayer = max(0,min(lin_bayer,1));
temp = uint16(lin_bayer*2^16);
lin_rgb = double(demosaic(temp,'gbrg'))/2^16;
warning('off', 'Images:initSize:adjustingMag');
%figure
%imshow(imrotate(lin_rgb,90));
redChannel = uint16(lin_rgb(:,:,1)*2^16);% Red channel
a = max(redChannel);
%figure
%imshow(imrotate(redChannel,90));
%imsave
greenChannel = uint16(lin_rgb(:,:,2)*2^16); % Green channel
b = max(greenChannel);
%figure
%imshow(imrotate(greenChannel,90));
%imsave
blueChannel = uint16(lin_rgb(:,:,3)*2^16); % Blue channel
```

```
c = max(blueChannel);
%figure
%imshow(imrotate(blueChannel,90));
%imsave
% Create an all black channel.
allBlack = zeros(size(lin_rgb, 1), size(lin_rgb, 2));
% Create color versions of the individual color channels.
just_red = cat(3, redChannel, allBlack, allBlack);
just_green = cat(3, allBlack, greenChannel, allBlack);
just_blue = cat(3, allBlack, allBlack, blueChannel);
grayim = rgb2gray(lin_rgb);
grayscale = 0.25/mean(grayim(:));
bright_srgb = min(1,lin_rgb*grayscale);
%imshow(imrotate(bright_srgb,90))
%imsave
```

APPENDIX B: MATLAB CODE FOR CALCULATING RADIALLY INTEGRATED SOOT VOLUME FRACTION

```
filename = 'filename.xlsx';   % filename of excel sheet output by Python code
radius = xlsread(filename,2,'B503:B564');  %radial location of flame
integrand = xlsread(filename,2,'E503:E564'); %local Soot volume fraction
integral = trapz(radius,integrand);
Fv  = integral/(3.14*(6^2))       %radial integration of soot volume fraction
```

APPENDIX C: PYTHON CODE

The following Python code has been referenced from Yale-CRP/Full 100 calculations.ipynb at master · DhrubajyotiDas/Yale-CRP · GitHub and was used to perform soot volume fraction calculations and plot their 2D distribution.

```
from __future__ import absolute_import
from __future__ import division
from __future__ import print_function
from __future__ import unicode_literals
from __future__ import division


import sys
import numpy as np
from numpy import savetxt
import scipy as sc
from scipy import optimize, signal, io, ndimage, constants, stats
from scipy.interpolate import InterpolatedUnivariateSpline
import itertools
import glob

import matplotlib.mlab as mlab
import customscripts as csc # Needed for 2-D Savitzky-Golay filter example at Scipy Cookbook

import os.path
import matplotlib.pyplot as plt
import abel

spa_rez = 40.69
S_TC_1=22123
S_TC_2=28834
T_TC_1=1573
T_TC_2=1643
tau_TC_1=1./30
tau_TC_2=1./30

def e_TC(l):
    answer = 1.2018e-6 * (l*1e9)**2 - (l*1e9) * 1.7167e-3 + 0.9017
    return answer

def soot_fv_calculator(T_soot, red_soot, tau_soot):
```

```
""" This function calculates the soot volume fraction
using flame luminosity, soot temperature, and an
independent absolute light calibration.

INPUTS:
-------
T_soot: Numpy array : 2D map of soot temperature
red_soot: Numpy array : BASEX inverted green channel of the flame image
tau_soot: float : Exposure time of the flame image

PARAMETERS:
-----------
S_TC_n : float : Luminosity of red channel of light calibration source
            (default source is a Type-S thermocouple)
            (n = 2 usually, i.e., images of the TC at 2 different temperatures is used)
T_TC_n : float : Temperature of the light calibration source
            (default is the self-reported TC temperature)
tau_TC_n : float : Exposure time of the light calibration source image
spa_rez : float : Spatial resolution of the camera setup in units of pixels per mm
             (For e.g., spa_rez = 28 means 28 pixels for every mm)

RETURNS:
--------
f_v_avg : Numpy array : 2D map of soot volume fraction
                at all physical locations for which both
                T_soot and green_soot information is available

                Multiply the output by 1e6 to convert to ppm

"""
lambda_S = 600e-9 # m, when used with e_TC(), it is converted to nm inside the function
K_ext = 8.6
L = 1e-3/spa_rez # m, dimension of 1 pixel, there being "spa_rez" pixels in every mm
e_TC_at_lambda_S = e_TC(lambda_S)
h = constants.Planck
c = constants.c
k = constants.Boltzmann

f_v_1 = (-1.0*lambda_S/(K_ext*L))*np.log(1 - e_TC_at_lambda_S
                    * (tau_TC_1 / tau_soot)
                    * (red_soot / S_TC_1)
                    * np.exp((-1*h*c/(k*lambda_S))
                            *(1/T_TC_1 - 1/T_soot)))

f_v_2 = (-1.0*lambda_S/(K_ext*L))*np.log(1 - e_TC_at_lambda_S
```

```
                    * (tau_TC_2 / tau_soot)
                    * (red_soot / S_TC_2)
                    * np.exp((-1*h*c/(k*lambda_S))
                            *(1/T_TC_2 - 1/T_soot)))

    f_v_avg = 0.5*(f_v_1 + f_v_2)

    return f_v_avg

Lookup_table_data = np.genfromtxt(r'C:\Users\abhee\Downloads\PyAbel-master\PyAbel-
master\examples\data\soot_lookup.txt')

Lookup_T = Lookup_table_data[:,0]
Interpolated_Lookup_bg = InterpolatedUnivariateSpline(Lookup_table_data[:,7], Lookup_T,
k=3)
Interpolated_Lookup_br = InterpolatedUnivariateSpline(Lookup_table_data[:,8], Lookup_T,
k=3)
Interpolated_Lookup_gr = InterpolatedUnivariateSpline(Lookup_table_data[:,9], Lookup_T,
k=3)

filename_red = os.path.join(r'C:\Users\abhee\Downloads\PyAbel-master\PyAbel-
master\examples\data','IBE30_0.2s_apr15_red_1.tif')
raw_data_red = plt.imread(filename_red).astype('float64')
raw_data_red1= np.zeros_like(raw_data_red)
raw_data_green1= np.zeros_like(raw_data_red)
raw_data_blue1= np.zeros_like(raw_data_red)

for x in range(20):
    filename_red = os.path.join(r'C:\Users\abhee\Downloads\PyAbel-master\PyAbel-
master\examples\data','IBE30_0.2s_apr15_red_'+str(x+1)+'.tif')
    filename_green = os.path.join(r'C:\Users\abhee\Downloads\PyAbel-master\PyAbel-
master\examples\data','IBE30_0.2s_apr15_green_'+str(x+1)+'.tif')
    filename_blue = os.path.join(r'C:\Users\abhee\Downloads\PyAbel-master\PyAbel-
master\examples\data','IBE30_0.2s_apr15_blue_'+str(x+1)+'.tif')

    raw_data_red = plt.imread(filename_red).astype('float64')
    raw_data_red1 += raw_data_red
    raw_data_green = plt.imread(filename_green).astype('float64')
    raw_data_green1 += raw_data_green
    raw_data_blue = plt.imread(filename_blue).astype('float64')
    raw_data_blue1 += raw_data_blue


raw_data_red_avg = raw_data_red1/20
raw_data_green_avg = raw_data_green1/20
raw_data_blue_avg = raw_data_blue1/20
```

```
raw_data_red1 = csc.sgolay2d(raw_data_red_avg,11,1)
raw_data_green1 = csc.sgolay2d(raw_data_green_avg,11,1)
raw_data_blue1 = csc.sgolay2d(raw_data_blue_avg,11,1)


red_flame =
abel.Transform(raw_data_red1,symmetry_axis=0,symmetrize_method='average',direction='inver
se',method='basex').transform
red_flame[red_flame<0]=0
green_flame =
abel.Transform(raw_data_green1,symmetry_axis=0,symmetrize_method='average',method='base
x',direction='inverse').transform
green_flame[green_flame<0]=0
blue_flame =
abel.Transform(raw_data_blue1,symmetry_axis=0,symmetrize_method='average',method='basex
',direction='inverse').transform
blue_flame[blue_flame<0]=0



center = blue_flame.shape[1]//2


red_flame = ndimage.filters.median_filter(red_flame, size = (1,9))
green_flame = ndimage.filters.median_filter(green_flame, size = (1,9))
blue_flame = ndimage.filters.median_filter(blue_flame, size = (1,9))



x = ndimage.filters.gaussian_filter(red_flame, 10, truncate=6.0)
mask_loose = np.ma.masked_where(x < 12, np.ones_like(x))
mask_tight = np.ma.masked_where(x < 12, np.ones_like(x))

masked_red_flame = np.ma.masked_where(np.ma.getmask(mask_loose), red_flame)
masked_green_flame = np.ma.masked_where(np.ma.getmask(mask_loose), green_flame)
masked_blue_flame = np.ma.masked_where(np.ma.getmask(mask_loose), blue_flame)


green_red = masked_green_flame / masked_red_flame
blue_red = masked_blue_flame / masked_red_flame
blue_green = masked_blue_flame / masked_green_flame
```

```
red_temp = Interpolated_Lookup_bg(blue_green)
green_temp = Interpolated_Lookup_br(blue_red)
blue_temp = Interpolated_Lookup_gr(green_red)


average_temp = (red_temp+green_temp+blue_temp)/3


soot_T = np.ma.masked_where(np.ma.getmask(mask_tight), average_temp)
print(np.mean(soot_T))



red_soot = np.ma.array(red_flame, mask = soot_T.mask)
tau_soot = 1.0/5.0

soot_fv = soot_fv_calculator(soot_T, red_soot, tau_soot)
print(np.mean(soot_fv))

nan_soot_T = soot_T.filled(fill_value=0)

nan_soot_fv = soot_fv.filled(fill_value=0)




savetxt('soot_fv_IBE30_0.2s_apr15_avg.csv', nan_soot_fv, delimiter=',')
#savetxt('soot_T_IBE90_0.33s_avg.csv', nan_soot_T, delimiter=',')




fig, ax = plt.subplots(ncols=2)
fig.set_size_inches(8.5,11)

y,x = blue_flame.shape

figure_x = x/spa_rez
figure_y = y/spa_rez
p_y, p_x = np.where(soot_fv == np.nanmax(soot_fv))

I1 = ax[0].imshow(soot_T,
                  vmin = 1800, vmax = 2000,
                  cmap = 'plasma', extent = [-0.5*figure_x, 0.5*figure_x, 0, figure_y])
fig.colorbar(I1, ax = ax[0])
```

```
ax[0].plot((x/2.-p_x)/spa_rez, (y-p_y)/spa_rez, 'o', mfc='None', ms=10, mew=1, mec='r',
zorder=4)

I2 = ax[1].imshow(soot_fv*1e6, vmin = 0, vmax = 0.25,
                  cmap = 'plasma', extent = [-0.5*figure_x, 0.5*figure_x, 0, figure_y])
fig.colorbar(I2, ax = ax[1])
ax[1].plot((x/2.-p_x)/spa_rez, (y-p_y)/spa_rez, 'o', mfc='None', ms=10, mew=1, mec='r',
zorder=4)




ax[0].set_title('Temperature (K)')
ax[0].set_xlabel('r (mm)')
ax[0].set_ylabel('HAB (mm)')
# axes[0].set_xlim(left=-4,right=4)
# axes[0].set_ylim(top=30)

ax[1].set_title('Soot volume fraction (ppm)')
ax[1].set_yticklabels([])
ax[1].set_xlabel('r (mm)')
# axes[1].set_xlim(left=-4,right=4)
# axes[1].set_ylim(top=30)

fig.tight_layout()
```

APPENDIX D: SOOT LOOKUP TABLE

The following is a lookup table for soot (soot_lookup.txt) that needs to be input into the Python code given in Appendix D to calculate soot volume fraction.

```
1000.0000000    0.0646000    0.0169000    0.2611000    1.0300000    0.9772000    1.0030000    0.0665380    0.0165147    0.2618833
1100.0000000    0.0843000    0.0263000    0.3115000    1.0260000    0.9742000    1.0033000    0.0864918    0.0256215    0.3125280
1200.0000000    0.1062000    0.0389000    0.3659000    1.0220000    0.9712000    1.0036000    0.1085364    0.0377797    0.3672172
1300.0000000    0.1300000    0.0550000    0.4235000    1.0180000    0.9682000    1.0039000    0.1323400    0.0532510    0.4251517
1400.0000000    0.1552000    0.0750000    0.4384000    1.0140000    0.9652000    1.0042000    0.1573728    0.0723900    0.4402413
1500.0000000    0.1814000    0.0988000    0.5447000    1.0100000    0.9622000    1.0045000    0.1832140    0.0950654    0.5471512
1600.0000000    0.2084000    0.1265000    0.6070000    1.0060000    0.9592000    1.0048000    0.2096504    0.1213388    0.6099136
1700.0000000    0.2359000    0.1580000    0.6697000    1.0020000    0.9562000    1.0051000    0.2363718    0.1510796    0.6731155
1800.0000000    0.2635000    0.1930000    0.7323000    0.9980000    0.9532000    1.0054000    0.2629730    0.1839676    0.7362544
1900.0000000    0.2912000    0.2313000    0.7945000    0.9940000    0.9502000    1.0057000    0.2894528    0.2197813    0.7990287
2000.0000000    0.3187000    0.2728000    0.8560000    0.9900000    0.9472000    1.0060000    0.3155130    0.2583962    0.8611360
2100.0000000    0.3458000    0.3170000    0.9166000    0.9860000    0.9442000    1.0063000    0.3409588    0.2993114    0.9223746
2200.0000000    0.3726000    0.3636000    0.9760000    0.9820000    0.9412000    1.0066000    0.3658932    0.3422203    0.9824416
```